Remote Sensing Applications: Society and Environment 38 (2025) 101624



Contents lists available at ScienceDirect

Remote Sensing Applications: Society and Environment

journal homepage: www.elsevier.com/locate/rsase



Integrated remote sensing and geophysical data for delineating the radioactive mineralization bearing-alteration zones, El-Missikat and El-Erediya areas, Central Eastern Desert, Egypt

Aya S. Shereif [a,b], Ali Shebl [a,b], Mahmoud Abdellatif [c], Mohamed A. Abdelkader [d,e], Mohamed Badawi [f,g], Abdelhalim S. Mahmoud [h], Árpád Csámer [a,i,*]

[a] Department of Mineralogy and Geology, University of Debrecen, Debrecen, 4032, Hungary
[b] Department of Geology, Tanta University, Tanta, 31527, Egypt
[c] Department of Geology, South Valley University, Qena, 83523, Egypt
[d] Department of Earth Resource Science, Graduate School of International Resource Sciences, Akita University, Akita, 010-8502, Japan
[e] Department of Geology, Faculty of Science, Menoufia University, Menoufia, 32513, Egypt
[f] Institute of Exploration Geosciences, University of Miskolc, Miskolc, 3515, Hungary
[g] Department of Geology, Mansoura University, Mansoura, 35516, Egypt
[h] Department of Geology, Fayoum University, Al-Fayoum, 63514, Egypt
[i] Cosmochemistry and Cosmic Methods Research Group, University of Debrecen, Debrecen, 4032, Hungary

ARTICLE INFO

Keywords:
Sentinel-2
PRISMA
Airborne geophysical data
Mineralization
Geological structures
SEM analysis

ABSTRACT

Relying exclusively on singular evidence nowadays is mostly insufficient for accurately identifying mineralized zones, particularly those hosting radioactive mineralizations. It is well-established that the integration of datasets leads to more reliable outcomes, particularly in the detection of potential mineralization deposits and the accurate discrimination of heterogeneous lithological units. Here, we combined multisource datasets like remote sensing data from Sentinel-2 and hyperspectral PRISMA with airborne geophysical data, encompassing magnetic and radiometric information. This study aims to meticulously investigate and map hydrothermal alteration zones associated with radioactive (uranium) mineralizations within the El-Missikat and El-Erediya regions. To accomplish this objective, satellite imagery underwent meticulous processing through a suite of techniques, including False Color Composites, Principal Component Analysis, Independent Component Analysis, Minimum Noise Fraction, and Band Ratios. Our study meticulously delineated the hydrothermal alteration zones associated with uranium deposition, including hematitization, epidotization, sericitization, and kaolinization. Furthermore, airborne geophysical findings provided insights into the spatial distribution of radioelements. In addition, the aeromagnetic findings highlighted the intricate structures that control mineralizations by depicting their depths via applying Tilt derivative (TD), Euler deconvolution (ED), and also distinctive mineralization sites through Center for exploration targeting (CET) grid analysis. Also, radiometric K/eTh ratio coupled with ternary composite maps of aeroradiometric data demarcated zones displaying potassic alteration that are associated with younger granitoids, proficiently differentiated radioactive mineralized zones, and different rock units, respectively. This integration is augmented through detailed fieldwork, petrographic analysis, and scanning electron microscopy (SEM). The latter confirmed the U-Th-REE-Nb-bearing minerals such as

* Corresponding author. Department of Mineralogy and Geology, University of Debrecen, Debrecen, 4032, Hungary
E-mail address: csamera@unideb.hu (Á. Csámer).

https://doi.org/10.1016/j.rsase.2025.101624
Received 4 January 2025; Received in revised form 8 May 2025; Accepted 10 June 2025
Available online 11 June 2025
2352-9385/© 2025 The Authors. Published by Elsevier B.V. This is an open access article under the CC BY license (http://creativecommons.org/licenses/by/4.0/).

zirconolite, euxenite-(Y) (polycrase-Y), and plumbo-pyrochlore (Pb-pyrochlore). Thus, we strongly advocate for the synergistic integration of remote sensing and geophysical datasets in future investigations to further refine mineral exploration strategies.

1. Introduction

Exploring minerals, especially radioactive ones, is crucial for boosting the economy and promoting sustainable development. Therefore, it is essential to prioritize exploring areas with these minerals and conduct detailed studies to discover significant deposits. The global community seeks advanced, cost-effective technologies to achieve this efficiently. It is widely acknowledged that the precise recognition and mapping of lithological units, delineation of the geological structures (faults, fractures, and shear zones), and improved monitoring of hydrothermal alteration zones constitute fundamental components crucial for accurately identifying sites of potential mineralizations (Mamouch et al., 2022; Sabins, 1999).

For more than four decades, spectral remote sensing technology has been a well-established tool in applied geology (Peyghambari and Zhang, 2021). The integration of varied remote sensing datasets (e.g., Sentinel-2, PRISMA, ASTER, PALSAR, OLI) played a vital role in effective delineation of regional and local structures, as well as distinguishing various lithological units (Pour and Hashim, 2015a, 2015b; Pournamdari et al., 2014a, 2014b). They have been extensively utilized in mineralizations and alteration zone detection (Frutuoso et al., 2021; Sabins, 1999). By employing spectral signature analyses and processing satellite images, we can differentiate between these alteration zones based on the distinctive characteristics exhibited by the detected mineral(s), particularly in the Visible and Near-Infrared (VNIR; 1300–185 nm) and Shortwave Infrared (SWIR; 1850–2600 nm) regions of the electromagnetic spectrum (Ghoneim et al., 2022; Pour and Hashim, 2012).

Geophysical data, including magnetic and radiometric information, have proven effective in identifying hydrothermal alteration zones associated with mineral deposits. Magnetic survey stands out as one of the initial techniques employed in mineral prospecting. Examining and enhancing aeromagnetic data enabled (1) the delineation of shallow and deep geological structure frameworks that control hydrothermal alterations, (2) the pinpointing of porphyry intrusion, (3) the reflection of the differences in lithological composition, lineaments, faults, contacts, crustal structures and degree of alteration (El-Dosouky et al., 2022; 2021, 2020; Elkhateeb and Abdellatif, 2018).

Airborne gamma-ray spectrometry data (AGRS) have proven to be highly effective in the exploration of potential areas enriched with radioactive elements (Hassan et al., 2022), environmental studies, geological mapping, and the identification of alteration zones (Elkhateeb and Abdellatif, 2018). All of these include mapping radioactive anomaly zones resulting from the presence of naturally occurring radioactive elements on the surface of lithological units, as well as monitoring the spatial distribution of these elements among different rock units within the study area. The latter encompasses potassium (K), equivalent uranium (eU), and equivalent thorium (eTh) (Darenely and Ford, 1989). This comprehensive investigation hinges on analyzing diverse factors, including variations in radiometric data, brightness Digital Number (DNs) values of rocks, predominant trends, densities of structural lineaments, as well as the shapes and types of weathering products (Hassan et al., 2022; Yousef, 2019).

The areas of El-Missikat and El-Erediya, situated in the Eastern Desert, are distinguished for harboring substantial mineralization deposits, encompassing sulfides (galena, pyrite, chalcopyrite, sphalerite, and molybdenite), barite, fluorite, copper, silver, and gold (Ammar et al., 2016). These areas stand out as some of the most substantial uranium reservoirs in Egypt's Eastern Desert (Hussein et al., 1986; Hussein and Sayyah, 1992), potentially harboring uranium resources of up to 8000 tons (Hussein et al., 1986), emphasizing their critical significance in the national economy. Accordingly, a large number of exploratory mining tunnels through the NW part of G. El-Missikat pluton and the southern part of G. El-Erediya pluton were dug (Abu-Deif and El-Tahir, 2008; El-Leil et al., 2015).

Geological structures, notably shear zones, exert a pivotal and influential role in determining and controlling the distribution of structurally controlled mineralizations, especially radioactive mineralization. The latter is closely associated with black and jasperoid veins within the shear zones (Abu-Deif et al., 1997; Hussein et al., 1986). These shear zones are situated in the northern part of the El-Missikat pluton, particularly along its interface with older granitoids (El-Leil et al., 2015), the northwestern part of the El-Maghrabiya region (El-Kammar et al., 2021), and the southern sector of the El-Erediya pluton, especially in proximity to the contact with metavolcanic rocks (Osman et al., 2005). The radioactive mineralization (U-bearing-mineralization) is associated essentially with hydrothermal alteration zones (argillic, phyllic, and propylitic) such as silicification, ferrugination, epidotization, and kaolinization (Hassaan et al., 2022).

The integration of remote sensing datasets with geophysical techniques has recently emerged as a powerful and reliable approach to enhance precision and efficiency in the precise differentiation of rock units, identification of shear zones, and mapping of alteration zones that harbor mineralizations (Abdelkareem et al., 2018; El-Dosouky et al., 2024; El-Qassas et al., 2023; S. M. Ghoneim et al., 2024; Saleh and Gabr, 2024).

This study aims to integrate high-resolution satellite imagery (e.g., Sentinel-2) with airborne geophysical data (magnetic and radiometric) for accurate assessment of the spatial distribution of radioactive mineralization in El-Missikat and El-Erediya regions. The approach focuses on delineating alteration zones and the precise identification of radioactive anomalies, specifically uranium point anomalies, embedded within the rock formations. As these areas frequently contain significant deposits of radioactive mineralization within the studied terrain, as well as the presence of surface and subsurface geological structures that control these zones and are associated with profitable mineralization resources. This investigation underwent rigorous verification through comprehensive field investigations, which involved the meticulous collection of samples from shear zones and mineralized granitic rock units. After this

fieldwork, a detailed petrographic investigation, as well as scanning electron microscopy and energy dispersive X-ray spectroscopy (SEM-EDX), was conducted. The cumulative evidence robustly supports the conclusion that samples derived from shear zones not only contain mineralization enriched in radioactive elements but also align with areas undergoing hydrothermal alteration. This provides conclusive evidence of a robust association between radioactive mineralization and alteration zones. Consequently, widely approved methodologies were employed for mapping and identifying potential alteration zones that harbor radioactive mineralizations.

2. Geological setting

2.1. Regional geology

The Arabian–Nubian Shield (ANS), making up the northern part of East Africa, is predominantly comprised of newly formed Neoproterozoic crust (Johnson et al., 2011; Johnson and Woldehaimanot, 2003; Stern, 2002) (Fig. 1). This crust formed during the evolution of both the arc and back-arc of the Gondwana continent, taking place in and around the margins of the Mozambique Ocean during the East African orogeny. The Arabian–Nubian Shield comprises four main rock sequences, including gneisses, metavolcanics, metasedimentary rocks, and granitoids.

The northwestern part of the Arabian-Nubian Shield is occupied by the Eastern Desert of Egypt (Sami et al., 2018). The Nubian Shield is categorized into the southern part (stretching from the Egyptian border to the Idfu-Marsa Alam road), the central part (located between the Idfu-Marsa Alam and Qena-Safaga asphaltic roads), and the northern domains (north of the Qena-Safaga road) (Hassaan et al., 2022) (Fig. 1).

The Central-northern sector of the Nubian Shield is recognized for its younger granite rocks, dating 550–610 Ma, which evolved during a period of extension of the Earth's lithosphere and include syenogranites, monzogranites, and alkali-feldspar granites. They are known for harboring significant metallic deposits, including gold, silver, fluorite, tin, tungsten, and molybdenum (Hassaan et al., 2022; Mahmoud et al., 2021), in addition to hosting a variety of rare metal mineralization such as columbite, cassiterite (El-Dokouny et al., 2023; Raslan, M. F., 2021) as well as significant uranium mineralization as reported by Ghoneim et al. (2024); Hassaan et al. (2022); Hussein et al. (1986); Hussein and Sayyah (1992); Raslan, M. F. (2021). Notably, all these mineralizations mentioned are present in younger granitic plutons and stocks like El-Missikat and El-Erediya in the central Eastern Desert (CED), as well as in G. Gattar and W-El-Faliq in the north and Um Ara in the south, as documented by Dawood and Abd El-Naby (2001).

2.2. Geology of the study area

The research area is located in the northern part of the Central Eastern Desert (CED) of Egypt and spans an area of approximately

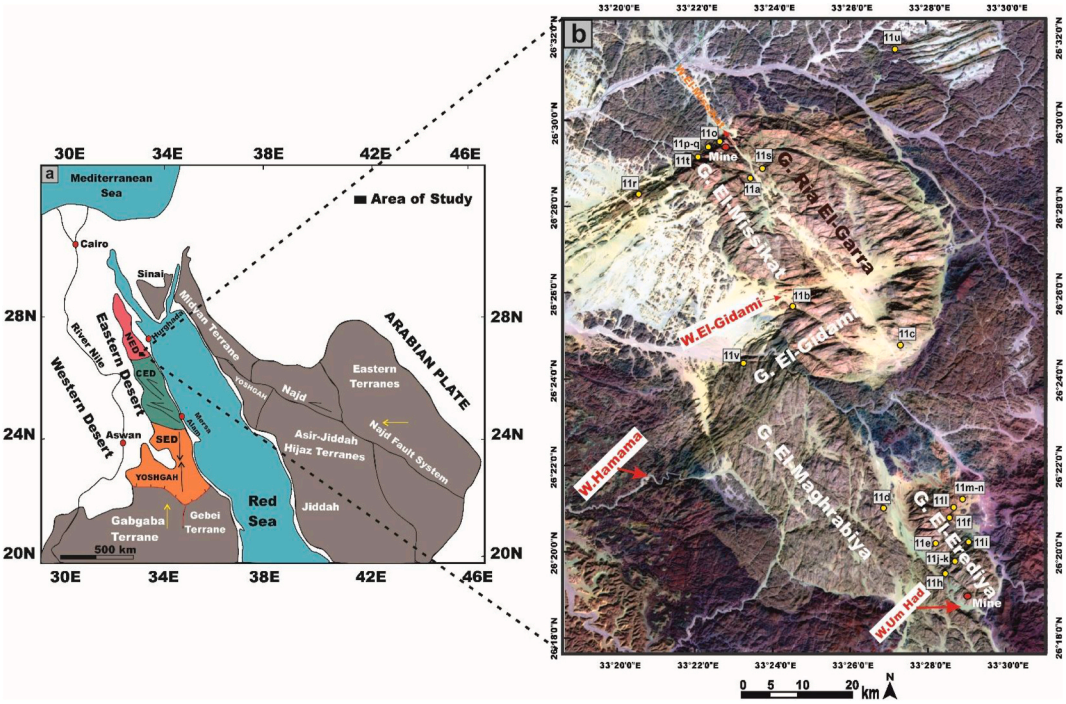


Fig. 1. (a) A simplified geological map of the Arabian Nubian Shield modified after Johnson et al. (2011); Johnson et al. (2011), showing the location of the study area (small black rectangle) and (b) location map of the study area (El-Missikat and El-Erediya), Central Eastern Desert, Egypt, with precise spatial distribution of field stations, related to Fig. 11.

576 km^2. It is located between latitudes 26°18′ and 26°32′ N and longitudes 33°20′ and 33°30′ E. This area is positioned approximately halfway between Qena in the Nile Valley and Safaga on the Red Sea shore (Fig. 1). The area under investigation is characterized by rugged topography with moderate to high relief.

The area hosts a rich tapestry of geological lithological units dating back to the Precambrian era, such as ophiolites (serpentinites, amphibolites, metagabbros, and metasediments), which represent the oldest rock units within the study area, island arc basic metavolcanic rocks, and younger gabbros, intermixed with acidic rock units, including island arc felsic metavolcanic rocks and syn-tectonic older granitoids (diorite, granodiorite, tonalities, and quartz diorite), followed by post-tectonic younger granitoids (monzogranites, syenogranites, and altered rich quartz granites). Nubian sandstone from the Early Cretaceous period forms an unconformable overlay atop all these rock units (Abd El-Naby, 2008; Amer, O., Kharbish, S., Maged, A., and Khedr, 2021; El-Leil et al., 2015; El Mezayen et al., 2017; Elsaid et al., 2014). The study regions are intricately crossed by a diverse network of fractures, with the NW-SE Najd Fault System notably standing out as prominent (El-Kammar et al., 1997).

It is worth noting that the study area includes post-orogenic younger granitoids, such as (1) G. El-Missikat pluton, which displays an ENE-WSW primary trend and a WNW-ESE secondary trend, (2) G. Ria El-Garra, demonstrating an ENE-WSW main trend and a NW-SE minor trend, functioning as the eastern part of G. El-Missikat, (3) G. El-Gidami, featuring ENE-WSW and NW-SE main trends and situated south G. El-Missikat pluton, (4) G. El-Maghrabiya, situated in the western part of G. El-Missikat, and lastly (5) G. El-Erediya, following a NW-SE main and a NE-SW minor trends, positioned in the southern part of G. El-Missikat and the southeastern part of G. El-Maghrabiya and G. El-Gidami. The four granite bodies (El-Missikat, Ria El-Garra, G. El-Gidami, and El-Erediya) were subjected to alteration processes such as argillic, propylitic, and phyllic (Hassaan et al., 2022), stretching from El-Erediya in the south to the northwestern boundary of El-Missikat, traversing through El-Gidami and Ria El-Garra.

Two significant strike-slip faults, oriented ENE-WSW and NW-SE, are observed at El-Missikat and El-Erediya, respectively, and demonstrate considerable displacement (Ammar et al., 2016). Notably, the youngest ENE-WSW strike-slip fault plays a pivotal role as a distinct boundary between the southern part of Ria-El Garra and El-Gidami, establishing a clear demarcation from El-Missikat (Hassaan et al., 2022; Osman et al., 2005). The oldest NW-SE fault trend separates the El-Erediya from the El-Missikat block and induces a relative displacement of the El-Erediya block towards southeast (Kassas and Bakhit, 1989).

The emplacement of the El-Missikat and El-Erediya granites in the Arabian-Nubian Shield is intricately tied to late-stage orogenic processes. Intense tectonic forces and compression caused crustal thickening, triggering partial melting of lower crustal rocks and generating granitic magmas rich in quartz, feldspar, and mica. These magmas ascended through structural dilations, intruding as plutons or batholiths, inducing thermal metamorphism and alterations in the surrounding country rocks.

The occurrence of these radioactive mineralizations in both regions is closely associated with the well-established shear zones related to younger granitoid plutons, which unquestionably play a pivotal structural role in governing the distribution and concentration of the radioactive minerals. They also play a crucial role in facilitating the flow of mineral-rich hydrothermal solutions (El-Leil et al., 2015). In the El-Missikat pluton, the dominant mineralization form is vein-type, extending primarily in an ENE-WSW direction. Conversely, within the El-Erediya pluton, the prevailing character of radioactive veins is the fracture-filling type, aligning predominantly along an NNW-SSE trend. The veins are predominantly filled with silica and exhibit a wide spectrum of variations ranging from common silica or jasperoid veins to ferruginous and siliceous mylonites occupying distinct fracture zones (Bakhit and Kassas, 1989).

3. Materials and methods

3.1. Remote sensing datasets (Sentinel-2 and PRISMA)

Sentinel-2, provided by the European Space Agency (ESA) under the Copernicus Programme, was launched on June 23, 2015 and March 7, 2017 (Ge et al., 2018b). Sentinel-2 provides spectral data spanning 12 bands at diverse spatial resolutions of 10, 20, or 60 m

Table 1
Characteristics of Sentinel-2 data.

Band Name (b)	Spatial Resolution/Pixel size (m)	Spectral region	Central Wavelength		Band Width (nm)	Purpose
			(μm)	(nm)		
B01	60	Ultra blue	0.443	443	20	aerosol detection
B02	10	Blue	0.490	490	65	blue
B03	10	Green	0.560	560	35	green
B04	10	Red	0.665	665	30	red
B05	20	VNIR	0.704	704	15	vegetation classification
B06	20	VNIR	0.740	740	15	vegetation classification
B07	20	VNIR	0.782	782	20	vegetation classification
B08	10	VNIR	0.842	842	115	near infrared
B08a	20	VNIR narrow	0.865	865	20	vegetation classification
B09	60	SWIR (WV)	0.945	945	20	water vapor
B10	60	SWIR cirrus	1.375	1375	30	cirrus
B11	20	SWIR	1.610	1610	90	snow/ice/cloud discrimination
B12	20	SWIR	2.190	2190	180	snow/ice/cloud discrimination

VNIR = visible near infrared, **SWIR** = short wave infrared.

(Bentahar and Raji, 2021) (Table 1). This precision enabled efficient identification of various alteration types, including ferric, ferrous iron, laterite, gossan, ferrous silicate, and ferric oxides (Ge et al., 2018a; Shebl et al., 2021). The preprocessing of Sentinel-2 data involved the transition to the Zone 36 North (UTM) projection, aligned with the WGS-84 datum. Subsequently, atmospheric correction was implemented to derive surface reflectance, employing the Sen2cor processor within the Sentinel Application Platform (SNAP).

PRISMA (Precursore IperSpettrale della Missione Applicativa), the sun-synchronous hyperspectral sensor of the Application Mission, PRISMA, was launched by the Italian Space Agency in March 2019. It offers 250 spectral channels across a wavelength range of 0.4–2.5 μm (Bedini and Chen, 2020; Loizzo et al., 2019; Mishra et al., 2022). PRISMA provides a wealth of spectral information in both the VNIR (66 channels from 400 to 1100 nm) and SWIR (174 channels spanning 920–2500 nm) regions. Exceptional signal-to-noise ratios exceeding 160, 100, and 240 are realized for VNIR, SWIR, and panchromatic channels, respectively. PRISMA functions as a push broom sensor, delivering a spatial resolution of 30 m for hyperspectral bands and 5 m for the panchromatic band. The latter encompasses a 30 km swath width and orbits at an altitude of 614.8 km with an inclination of 97.751° (Loizzo et al., 2019) (Table 2).

To date, the geological uses of PRISMA images encompass (1) lithological mapping (Shebl et al., 2023, 2024), (2) mapping of hydrothermal alteration assemblages, and (3) outlining the spatial arrangement of alteration minerals (Bedini and Chen, 2020).

The source of Sentinel-2 and PRISMA datasets was attained through the **ESA open data hub** and https://prisma.asi.it/missionselect/, respectively. The acquisition date of the remote sensing datasets utilized in this study corresponds to September 2023.

The materials and methodologies followed in this study are illustrated in the flowchart in Fig. 2.

3.2. Image processing techniques

In this study, a diverse range of image processing techniques has been employed. These methods encompass Principal Component Analysis (PCA), Independent Component Analysis (ICA), False Color Composites (FCCs), Band Ratio (BR), and Minimum Noise Fraction (MNF) (Table 3). These methods have proven successful globally in lithological and alteration zone mapping on multispectral and hyperspectral satellite imagery (Salem, 2013).

3.3. Airborne geophysical data

The airborne geophysical survey, in terms of aeromagnetic and aeroradiometric measurements of the area, was involved in the study. The survey was performed by the Aero-Service Division, Western Geophysical Company of America, in 1984, for the Egyptian Geological Survey and Mining Authority (Aero-Service, 1984). The datasets are available in the form of total magnetic intensity (TMI), potassium (K), equivalent thorium (eTh), and equivalent uranium (eU) concentration contour maps. The maps are digitized, gridded, and interpolated using minimum curvature techniques, and the final form of the raw data is displayed in colored gridded maps in Fig. 8a, b, c, and d.

Quite a few enhancement filters (maps) under the terms of (1) Tilt angle Derivative "TD" (Miller and Singh, 1994), relies on ratio of potential derivatives where $TD = \tan^{-1}(FVD/HD)$ for well enhancing of small and large amplitude anomalies. (2) Euler deconvolution "ED" (Reid et al., 1990), involving the orthogonal gradients of the potential field where $(x - x_0)\frac{\partial t}{\partial x} + (y - y_0)\frac{\partial t}{\partial y} + (z - z_0)\frac{\partial t}{\partial z} = N(B - T)$; N is the Structural index, and B is the field base level, T is the measured field. The method is greatly effective in depicting the depths of magnetic anomalies. (3) Centre for exploration targeting (CET) grid analysis (Holden et al., 2008). Including a group of filters (e.g., Entropy which measures the data randomness based on the probability, phase symmetry for revealing line-like structure via recognizing axes of symmetry, vectorization for generating skeletal features and converting them into lines, the intersections of these lines include junctions, crossings, and corners are used as input for producing contact occurrence density map (Figs. 9 and 10a, and b). (4)

Table 2
Characteristics of PRISMA Satellite data (Loizzo et al., 2019).

Parameter	VNIR Channel	SWIR Channel	PAN Channel
Spectral range	400–1010 nm	920–2500 nm	400–750 nm
Spectral resolution, Full Width Half Maximum (FWHM)	12 nm	12 nm	–
Spectral bands	66	171	1
Signal-to-Noise Ratio (SNR)	>200 in the range 400–1000 nm >600:1 @ 650 nm	>200 in the range 1000–1750 nm >400 @ 1550 nm >100 in the range 1950–2350 nm >200 @ 2100 nm	>240
Modulation Transfer Function (MTF)	@ Nyquist Frequency >0.3	@ Nyquist Frequency >0.3	@ Nyquist Frequency >0.2
Swath width	30 km (FOV = 2.77°)		
Spatial resolution	30 m		5 m
Telescope aperture	210 mm (diameter)		
Orbital altitude	620 km		
Telescope Type	TMA (Three-Mirror Anastigmat)		
Spatial detector Pixels	1000*256 with 30 μm pitch		6000
Instantaneous Field of View (IFOV)	48.34 μrad		

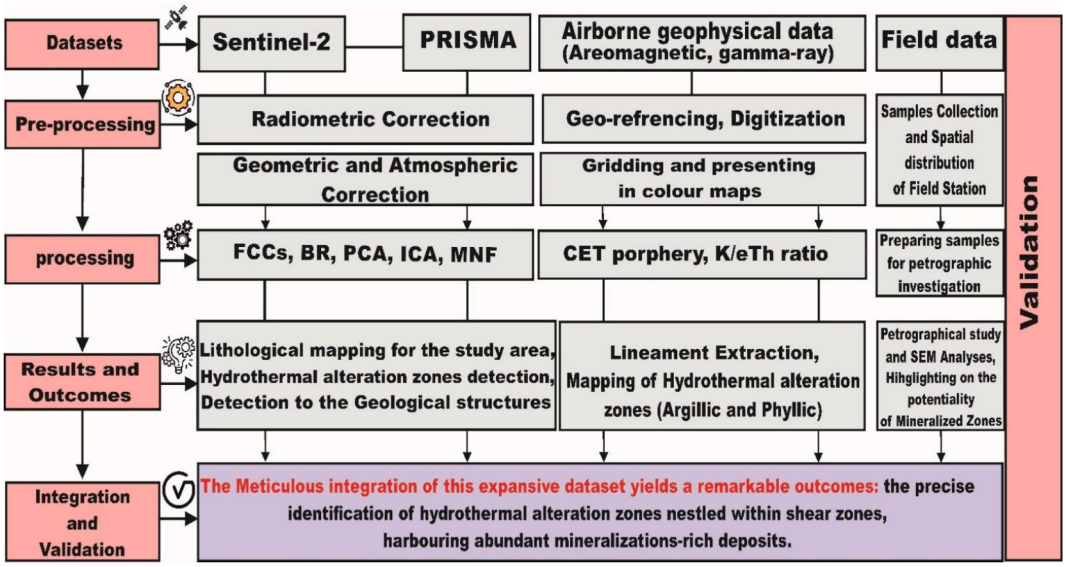


Fig. 2. A flow chart depicting the methodology of this study.

k/eTh ratio, and ternary composite maps of the aeroradiometric measurements clearly revealed areas of potassic alteration, high radioactive sites, and also distinguished different lithological units (Fig. 10c and d).

The focal intention of the airborne geophysical data is to assist in identifying the criteria (e.g., structures and their depths, hydrothermal alteration, and lithological mapping) that are strongly related to the promising mineralized localities.

3.4. Sampling preparation and processing

Sheared, altered, and mineralized samples were systematically collected from the El-Erediya granitic pluton to identify alteration zones associated with radioactive mineralization. Sampling focused on two distinct areas, the shear zone in the southern section of the pluton (sheared granite) and regions distant from the shear zone (unsheared granite). These samples were meticulously prepared as thin sections and analyzed under a Nikon polarizing microscope to examine their intricate mineralogical compositions and textural characteristics. Following this initial microscopic evaluation, selected samples exhibiting pronounced shearing or evidence of radioactive mineralizations underwent advanced analysis using an Environmental Scanning Electron Microscope (ESEM). Backscattered electron (BSE) imaging, paired with Energy-Dispersive X-ray Spectroscopy (EDX), was employed to determine the elemental composition of individual minerals. All laboratory analyses were conducted with precision at Akita University, Japan.

4. Results

4.1. Remote sensing data

4.1.1. Precise lithological mapping

The utilization of MNF 8 technique on PRISMA satellite images has showcased an impressive ability to discern between acidic and basic rock units within the El-Missikat and El-Erediya area (Fig. 3a). This capability has greatly advanced our comprehension of the study region and affirmed the findings of prior investigations that identified its diverse geological compositions (Abd El-Naby, 2008; Amer, O., Kharbish, S., Maged, A., and Khedr, 2021; El-Leil et al., 2015; El Mezayen et al., 2017; Elsaid et al., 2014).

As well as, the satellite emerged as a pivotal and unequivocal tool to precisely delineate areas where ophiolites, particularly the distinctive amphibolite rocks, are conspicuously manifested (Fig. 3b) by applying the PC2 technique. These delineated regions correspond to sites scrutinized in earlier research, wherein their ophiolitic nature was affirmed, providing robust evidence for their inclusion in the lithological mapping (Fig. 3b).

This satellite demonstrates and impeccably illustrates the stark contrast between older granitoids rocks and their contemporary counterparts of younger granitoids (Fig. 3c), by applying IC9. The nuanced gradations of color within each unit vividly emphasize the distinctions and diversity inherent within granite units, aligning seamlessly with findings from prior research. Each collection of syntectonic older granites (Abd El-Naby, 2008; El-Leil et al., 2015; Elsaid et al., 2014)and post-tectonic younger granites (Abd El-Naby, 2008; Bakhit and Kassas, 1989; El Mezayen et al., 2017; Elsaid et al., 2014; Kassas and Bakhit, 1989) contains specific types, as we described previously.

Delving deeper into the intricate details of the study area, the PRISMA satellite images have played a pivotal role in definitively distinguishing younger granitoid rocks in the El-Missikat and El-Erediya areas, effectively delineating between monzogranites and

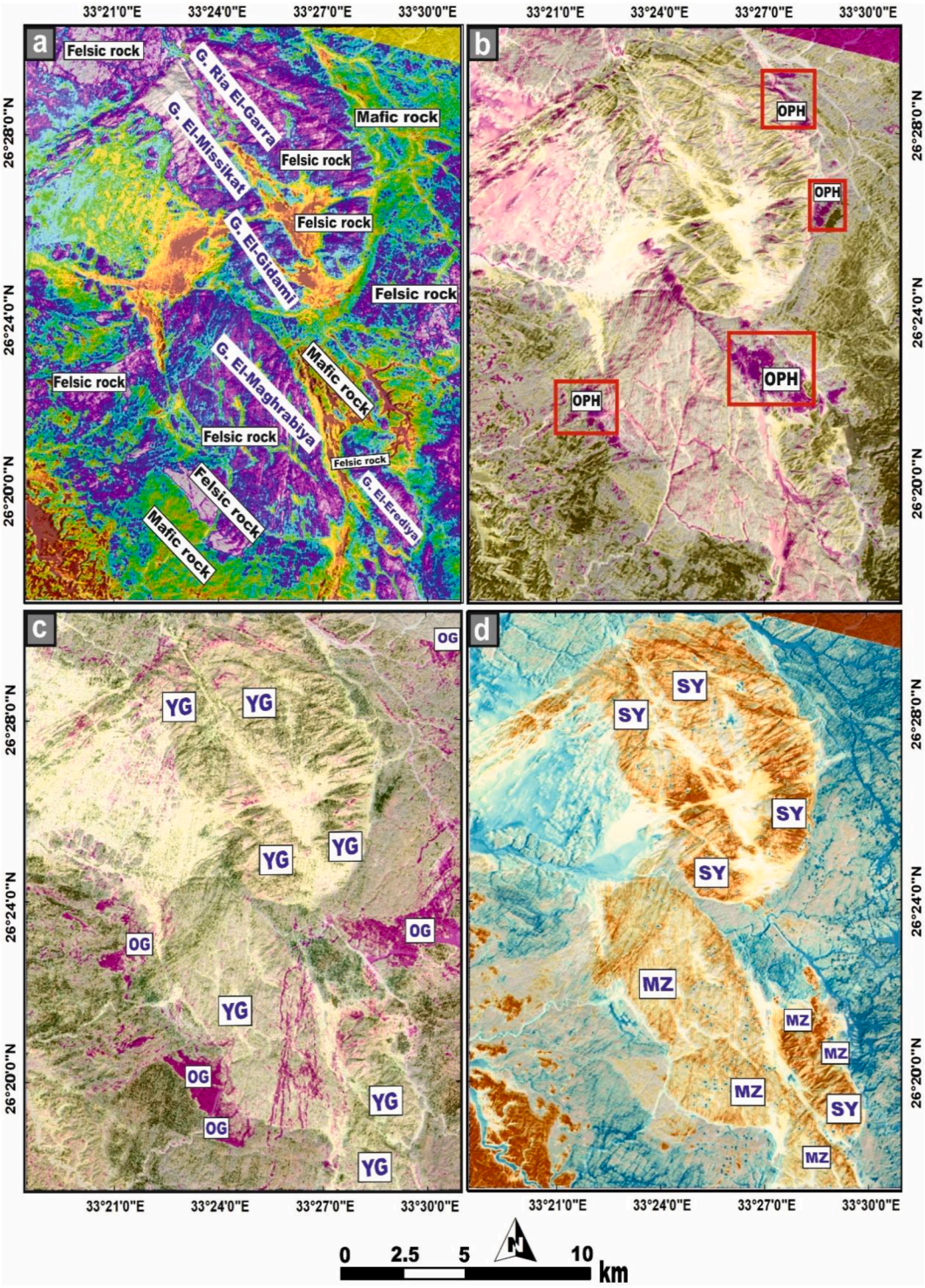


Fig. 3. A colored representation of PRISMA satellite images showing (a) MNF 8, which provides a detailed differentiation between acidic and basic rock units within the El-Missikat and El-Erediya area, (b) PC2, which provides a comprehensive illustration of the distribution of ophiolite group (OPH), highlighting the specific locations of amphibolite rocks that belong to this group, (c) IC9 vividly delineates the contrast between older and younger granitoids (OG and YG) and (d) PC4 elucidates the distinctions between younger types of granites, specifically monzogranites (MZ) and syenogranites (SY).

Table 3
Image processing techniques of remote sensing data utilized in our study.

Method	How does it work in our study?	Objectives of our study	Definition
False color composites (FCCs)	A specialized FCC using (12/6/2) band combinations in RGB on Sentinel-2 imagery was employed.	To generate a visually enhanced representation, facilitating the detailed mapping and precise discrimination of lithological units within El-Missikat and El-Erediya regions (Fig. 1).	FCCs are powerful tools for interpreting raster data across visible and invisible wavelengths (Nafigin et al., 2022). Selecting specific spectral bands enhances the differentiation of geological structures, lithological units, and hydrothermal alteration zones, which are represented by distinct colors and gradients (Campbell and Wynne, 2011). Variations in the color spectrum for identical band combinations across study areas reflect differences in sedimentation environments and rock mineral composition.
Principal Components Analysis (PCA)	We employ PCA on PRISMA imagery like PC2 and PC4 components	To enhance the visual clarity of satellite imagery, enabling more precise differentiation between lithological units and geological structural features associated with mineralizations in the shear zones (Fig. 3b–d, and 4b).	PCA is a statistical technique that reduces correlations among satellite imagery bands into uncorrelated principal components by identifying orthogonal axes that maximize data variance (Hassan and Ramadan, 2015). This method enhances the detection of distinct factors linked to specific mineral classes (Ranjbar, 2011). The Crosta technique, introduced by Crosta and Moore (1989) and later refined (Crosta et al., 2003), applies PCA to generate mineralization maps using high spectral resolution data.
Independent Component Analysis (ICA)	We employ PCA on PRISMA imagery like IC9, IC10 and IC6 components	For accurate lithological differentiation, facilitate detailed mapping of hydrothermal alteration zones and delineate structural features intricately associated with mineral assemblages (Fig. 3c and 4c, and d).	ICA is an extension of PCA (Tharwat, 2021), which identifies statistically independent components rather than merely uncorrelated ones by transforming multidimensional random vectors into independent signals. ICA effectively detects elements of interest within images, even if they constitute a small fraction of pixels or are obscured by noise (Pour et al., 2019). This method leverages blind source separation (BSS) during data whitening (Lee et al., 2000) and utilizes higher-order statistics to reveal intricate features (Hyvärinen and Oja, 2000).
Minimum Noise Fraction (MNF)	We employ MNF on PRISMA imagery, like MNF 8 and MNF6	To effectively differentiate lithological units, identify structural features associated with mineralizations, and discriminate hydrothermal alteration zones (Fig. 3a and 4a).	This approach identifies deviations in spectral patterns that commonly indicate alterations resulting from hydrothermal mineralization (Ge et al., 2018), which is important for exploratory geologists. It organizes components in ascending order of random noise rather than descending order of variance in principal components (Assiri, 2016). MNF is a linear transformation that consists of two consecutive PCA transformations (Nafigin et al., 2022). Initially, in the noise whitening stage, the main components for the noise covariance matrix are computed, resulting in decorrelation and data rescaling. In the subsequent stage, the main components are derived from the noise-whitened data, involving a split into two parts: one associated with large eigenvalues and the other with near-unity eigenvalues and noise-dominated images. The incorporation of large eigenvalues aids in separating noise from the data, ultimately improving the results (Pour and Hashim, 2012).
Band ratios (BR)	We employ BR on Sentinel-2 imagery like the Sabins ratio (4/2)	For mapping of iron oxide/hydroxide minerals such as ferric, ferrous oxides, laterite, gossan, and ferrous silicates (Fig. 5).	Band ratios are a powerful technique for identifying and mapping hydrothermal alteration minerals and lithological units by enhancing specific spectral responses with improved precision (El-Dosouky et al., 2020; Pour and Hashim, 2012a). This method involves applying mathematical operations to multispectral images to reduce spectral reflectance variations caused by topography or seasonal sunlight changes (Crippen et al., 1988). By dividing the digital number (DN) values of one band by those of another, band ratios effectively highlight mineral-specific features. Visible and near-infrared (VNIR) bands

(*continued on next page*)

Table 3 (*continued*)

Method	How does it work in our study?	Objectives of our study	Definition
			(0.45–1.2 μm) are particularly useful for identifying iron oxide/hydroxide minerals, as they provide critical diagnostic information on Fe^{3+}/Fe^{2+} transitions (Clark, 1999).

syenogranites (Fig. 3d). This discovery aligns seamlessly with previous studies that have verified the presence of syenogranites in the El-Missikat, El-Erediya, Ria El-Garra, and El-Gidami areas while identifying monzogranites in the El-Maghrabiya and the northern part of El-Erediya (Abd El-Naby, 2008; Bakhit and Kassas, 1989; El Mezayen et al., 2017; Elsaid et al., 2014; Kassas and Bakhit, 1989).

4.1.2. Mineralogical indices for radioactive mineralization detection

Fig. 4a offers detailed insights into shear zones associated with younger granitoid plutons and reveals numerous alterations, facilitating the straightforward identification of mineralizations. These findings have been extensively validated and elucidated in prior studies (Abdel-Hakeem et al., 2023; Bakhit and Kassas, 1989; Osman et al., 2005), which confirms the accurate placement of the shear zones in their respective locations. Furthermore, Fig. 4a depicts the weathering and alteration of all syenogranites in the El-Missikat, Ria El-Garaa, El-Gidami, and El-Erediya areas. It is worth noting that previous studies have consistently supported these observations (Abdel-Hakeem et al., 2023; Bakhit and Kassas, 1989; El-Kammar et al., 2021).

Continuing the investigation into shear zones within the study area, Fig. 4b provides additional clarity. It reveals the veins within the shear zones and the granite units serving as hosts for fluorite mineralizations, especially in the western section of G. El-Maghrabiya (Fig. 4b). Extensive research supports the assertion that the regions highlighted in the imagery are characterized by highly sheared granitic rocks or veins containing fluorite (Abd El-Naby, 2008; Amer, O., Kharbish, S., Maged, A., and Khedr, 2021; El-Kammar et al., 2021; El-Leil et al., 2015).

PRISMA data, utilizing the IC10 technique, has reaffirmed the phenomenon of K-metasomatic alteration, which happened to high potassium-calc alkaline granitoids in the study area, that previously documented in earlier studies (Abdel-Hakeem et al., 2023; Abu-Deif et al., 1997), thereby enhancing the robustness and credibility of our findings (Fig. 4c). An alternative interpretation of Fig. 4c prompts us to consider its implications of uranium (radioactive) mineralization. Previous studies have firmly established that these younger syenogranites are uraniferous granites (El-Leil et al., 2015).

Extensive research has consistently affirmed the presence of various types of mineralization deposits. These inquiries extend beyond radioactive mineralizations. Notable among these mineralizations are sulfides (such as molybdenite, pyrite, galena, chalcopyrite, and sphalerite), gold, and fluorite, as well as valuable ores like cassiterite (tin ore) and tungsten ores (wolframite and scheelite). Previous studies have established the existence of these mineral occurrences in proximity to magmatic zones (intrusion zones) in the El-Missikat and El-Ereidya regions or the form of Wadi sediments (Abdel-Hakeem et al., 2023). Fig. 4d, utilizing the IC6 technique on PRISMA, offers further validation of the presence of these minerals, with squares marking their concentration in the vicinity of younger granitoids.

4.1.3. Detection and delineation of hydrothermal alteration zones

Building on prior studies, the alteration zones within the shear zones predominantly host hydroxyl-bearing mineralizations. Notably, uranium minerals often coexist with these minerals. We confirmed these findings using Sentinel imagery in tandem with Sabins technique, highlighting the dominant alteration types in these areas (Fig. 5a).

Remote sensing techniques identified various secondary minerals, including hydroxyl-bearing minerals, including clay minerals (kaolinite, illite), hydroxides (goethite, hematite, gibbsite, brucite), carbonates (calcite, dolomite), and phyllosilicates (micas like muscovite and biotite, chlorites). Upon comparing hydroxyl-bearing mineralizations and alteration zones in the study area, a clear pattern emerges, nearly all hydroxyl minerals originate within alteration zones, with a pronounced concentration observed in shear zones (Fig. 5a), highlighted within squares. To elucidate each type of hydroxyl-bearing mineralization individually, Sentinel-2 satellite images provide distinct visual representations for each (Fig. 5b, c, and d).

Iron oxides, such as hematite, limonite, goethite, and manganese, often appear as stains, patches, or dendritic formations and are key indicators of hydroxyl mineralization, particularly hematization alteration (Abdel-Hakeem et al., 2023; Abu-Deif and El-Tahir, 2008; El-Kammar et al., 2021; El-Leil et al., 2015; Hassaan et al., 2022; Hussein et al., 1986). Sentinel-2 imagery confirmed these findings, identifying hematization and manganese alterations along siliceous veins, fractures, and sheared granitic rocks (Fig. 5b).

Fig. 5c illustrates gossan ore within the study area, predominantly occurring in granitic rocks and notably abundant within shear zones.

Fig. 5d adeptly pinpointed the kaolinization and sericitization alteration zones, notable for their abundance of hydroxyl-bearing mineralizations. These alterations are especially prominent, particularly at the intersection of mineralized silica veins with younger granite formations. This correlation has been confirmed in previous research (Abdel-Hakeem et al., 2023; Abu-Deif and El-Tahir, 2008; Ammar et al., 2016; El-Leil et al., 2015) and is further validated with precision by the Sentinel-2 satellite image (Fig. 5d).

4.1.4. Delineation of structural features

Satellite (Sentinel-2 and PRISMA) images have proven invaluable in uncovering not only mineralization patterns but also shedding light on the prevailing geological structures in the region, which play a significant role in shaping the distribution of these

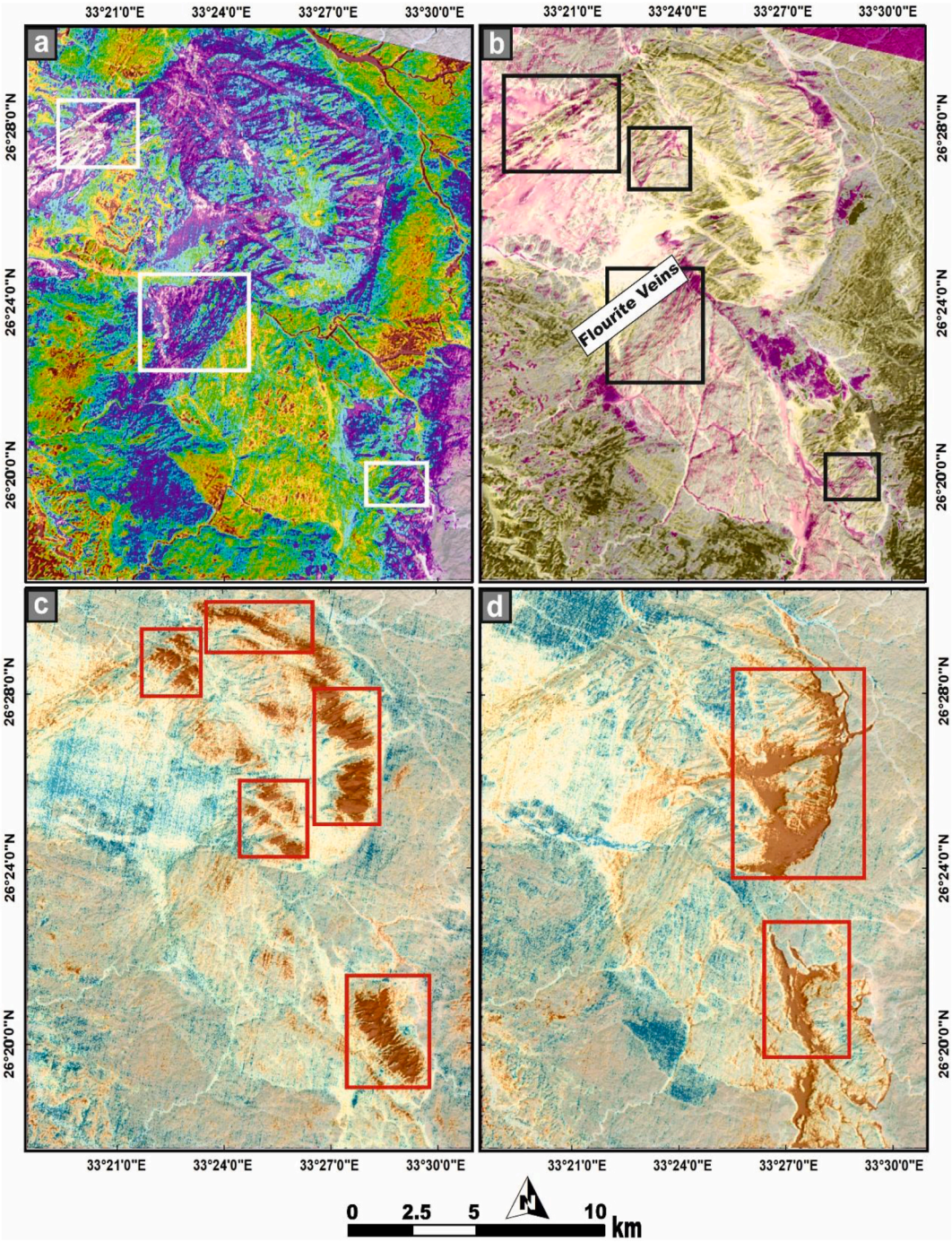


Fig. 4. PRISMA satellite images, (a) Pseudocolor map of MNF6, provides a clear depiction of shear zones, along with evident signs of erosion and weathering affecting the younger granites in the area, particularly syenogranites (b) Pseudocolor map of PC2, clearly delineates the veins and highly sheared granite-bearing fluorite, particularly prominent within the shear zones (C) Pseudocolor map of IC10, effectively illustrates K-metasomatic alteration (K-metasomatism) occurring on the surface of syenogranite units and (d) Pseudocolor map of IC6, showcases the diverse mineralizations surrounding the El-Missikat and El-Erediya plutons, including sulphides, gold, fluorite, cassiterite and tungsten ores. All of these previous features are highlighted with colored rectangles.

mineralizations (Fig. 6a–e). Within our study area, a diverse array of geological structures is discernible, with notable attention drawn to the shear zones that were highlighted in a previous image (Fig. 4a). These images (Fig. 6a–e) also reveal these intricate structural details consistent with earlier research and studies (El-Leil et al., 2015).

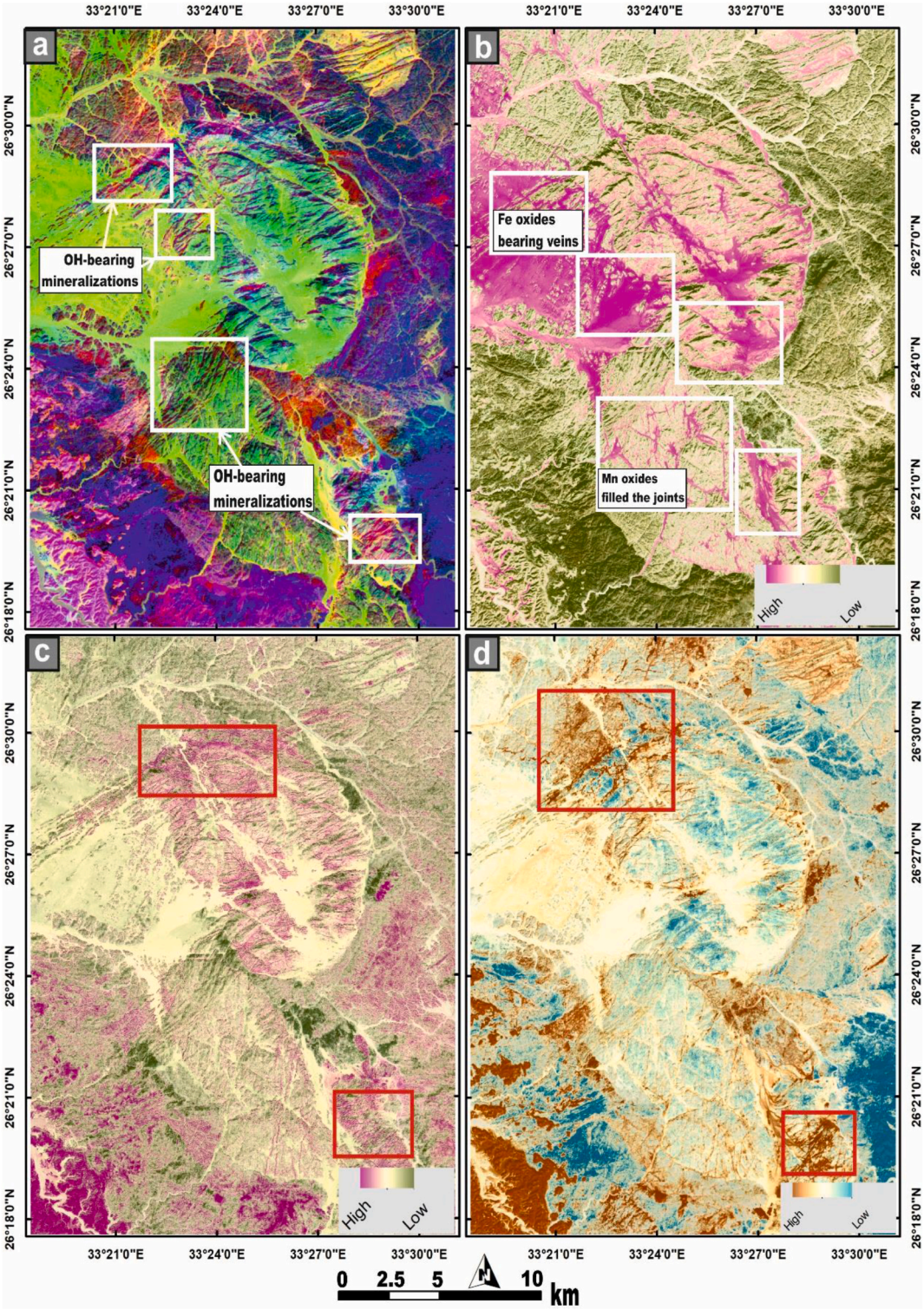


Fig. 5. Sentinel-2 satellite images showing, (a) Sabins ratio highlighting the main alteration pattern present in the study area, (b) effectively highlights iron-bearing minerals or areas of Fe-bearing alteration, (c) effectively delineates the areas containing gossan and (d) demonstrates a clear differentiation between two types of alteration zones containing hydroxyl-bearing mineralizations, namely kaolinitization and sericitization, effectively isolating them from the iron-bearing alteration zones. All of these features are marked with colored rectangles.

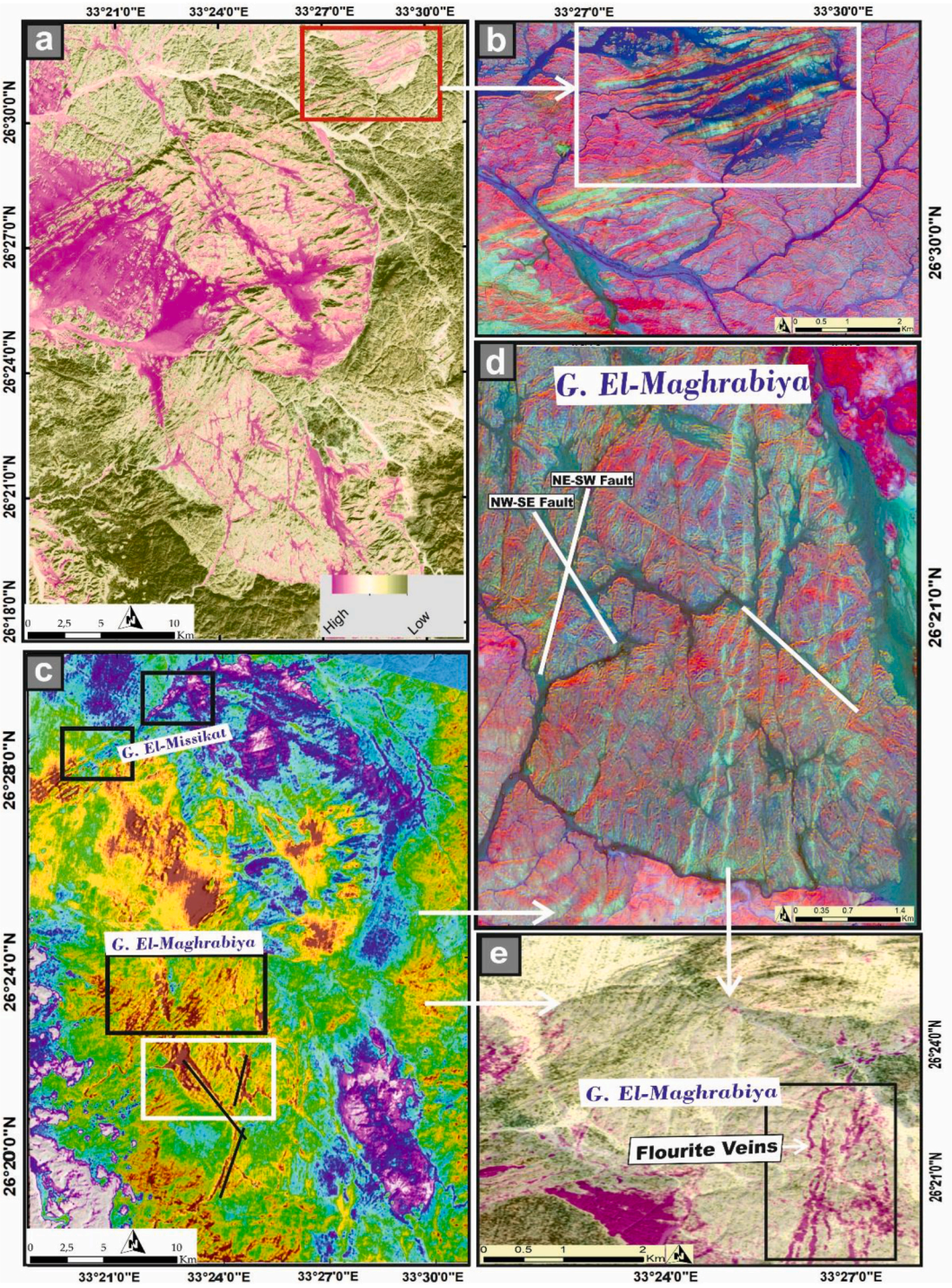


Fig. 6. Sentinel-2 and PRISMA satellites images, (a) shows a small view to the felsite dykes swarms positioned in the NE corner of the surveyed area, (b) shows an close-up (enlarged) view of the same dykes swarms, (c) in a concise view, reveals the presence of aplite dyke swarms cutting through the NW section of the El-Missikat pluton, alongside quartz-feldspar porphyry dyke swarms intersecting the NW portion of the El-Maghrabiya pluton. Additionally, it highlights discontinuities, joints, and fractures within the latter pluton, along with doleritic dykes following the same orientation of the faults penetrating El-Maghrabiya pluton, (d) enhanced magnified view of the joints and fractures within El-Maghrabiya, accompanied by the directional indicators of faults and (e) offers a detailed view of the fluorite-bearing veins that bisect the El-Maghrabiya pluton. All of these features are distinctly marked with colored rectangles.

By employing Sentinel-2 imagery, felsite dyke swarms, in the NE boundary of the El-Missikat granitic pluton are depicted and delineated in Fig. 6a at a small scale and in Fig. 6b with an enhanced and magnified perspective. This correlation aligns with the previous studies (El-Kammar et al., 2021). These dykes exhibit pronounced dislocation along a NW-SE-oriented sinistral fault (Fig. 7).

In the NW section of El-Missikat, by utilizing PRISMA image, aplite and lamprophyric dike swarms are depicted and confirmed in Fig. 6c. This finding aligns with the prior studies (El-Leil et al., 2015).

In the NW periphery of G. El-Maghrabiya, quartz-feldspar porphyry dyke swarms, oriented NE-SW to ENE-WSW, intersect the area, spanning lengths of up to 8 km and widths of up to 20 m (El-Kammar et al., 2021). This is depicted in Fig. 6c using the PRISMA satellite image. G. El-Maghrabiya pluton exhibits cavernous, exfoliated, jointed, and fractured characteristics, with manganese oxides filling joints and fractures. These observations align with previous studies (El-Kammar et al., 2021) and are substantiated by satellite imagery from both PRISMA satellites (Fig. 6c) and in an enlarged perspective using Sentinel-2 (Fig. 6d).

Doleritic dykes in the El-Maghrabiya area trend NE-SW, NW-SE and E-W, with vertical to steep inclinations aligned with fault trends. These dikes typically exhibit straight formations with subtle curvatures and ranging from 0.5 to 10 m in thickness and extending several kilometers, include the NW-SE dykes, which are the youngest in the region (El-Kammar et al., 2021). Sentinel-2 and PRISMA imagery (Fig. 6c and d) further confirm these characteristics. Additionally, fluorite veins, associated with uranium deposits, are highlighted in Fig. 6e. This correlation was previously examined by Amer et al. (2021) and confirmed through Sentinel-2 and PRISMA satellite image analysis (Fig. 6d and e).

Generally, the emplacement of El-Missikat and El-Erediya granites and other related features, i.e., dikes and conjugate fault sets, indicates sequential deformational phases developing brittle or ductile solid-state deformation, particularly at a brittle phase. The emplacement of these granites is related to the NW-SE Najd Fault System (NFS), which is the master shear array in the CED of Egypt (Hassaan et al., 2022). They evolved into intricately fractionated granites after the maturation of the continental crust, occurring concurrently with D3 crustal extension as a late extensional regime. Following crystalline relaxation, these granites underwent subsequent intersecting by numerous fractures and dikes, predominantly oriented in the ENE and NE directions, respectively. The first phase set of dikes arose due to extension along the NW-SE axis, subsequently undergoing left-lateral displacement purportedly associated with NFS (Fig. 7). Later, the second phase exhibits a notable enrichment in fluorite and is conjectured to stem from dextral reactivation at shallow crustal depths. On the contrary, these dikes, especially at the contact between G. El-Gidami and G. El-Maghrabiya, show S-shape bending (Fig. 7), suggesting they developed within a ductile state deformation.

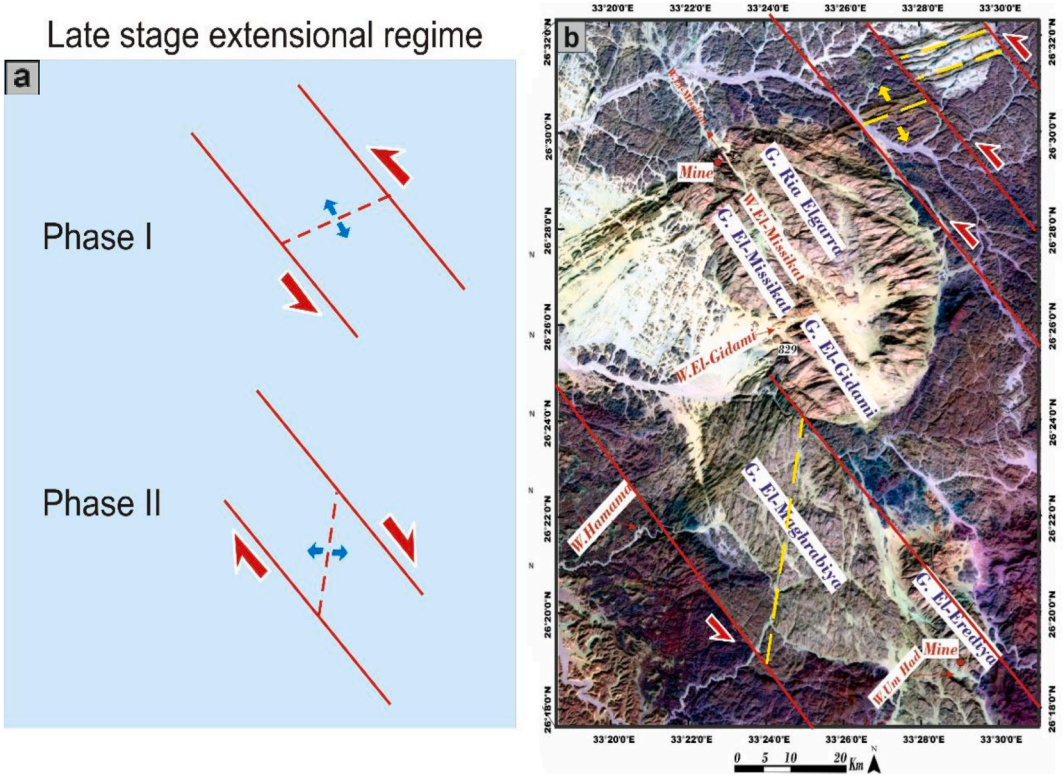


Fig. 7. (a–b) Sentinel-2 satellite image showing structural trends controlling El-Missikat and El-Maghrabiya plutons and related late-stage extensional fractures.

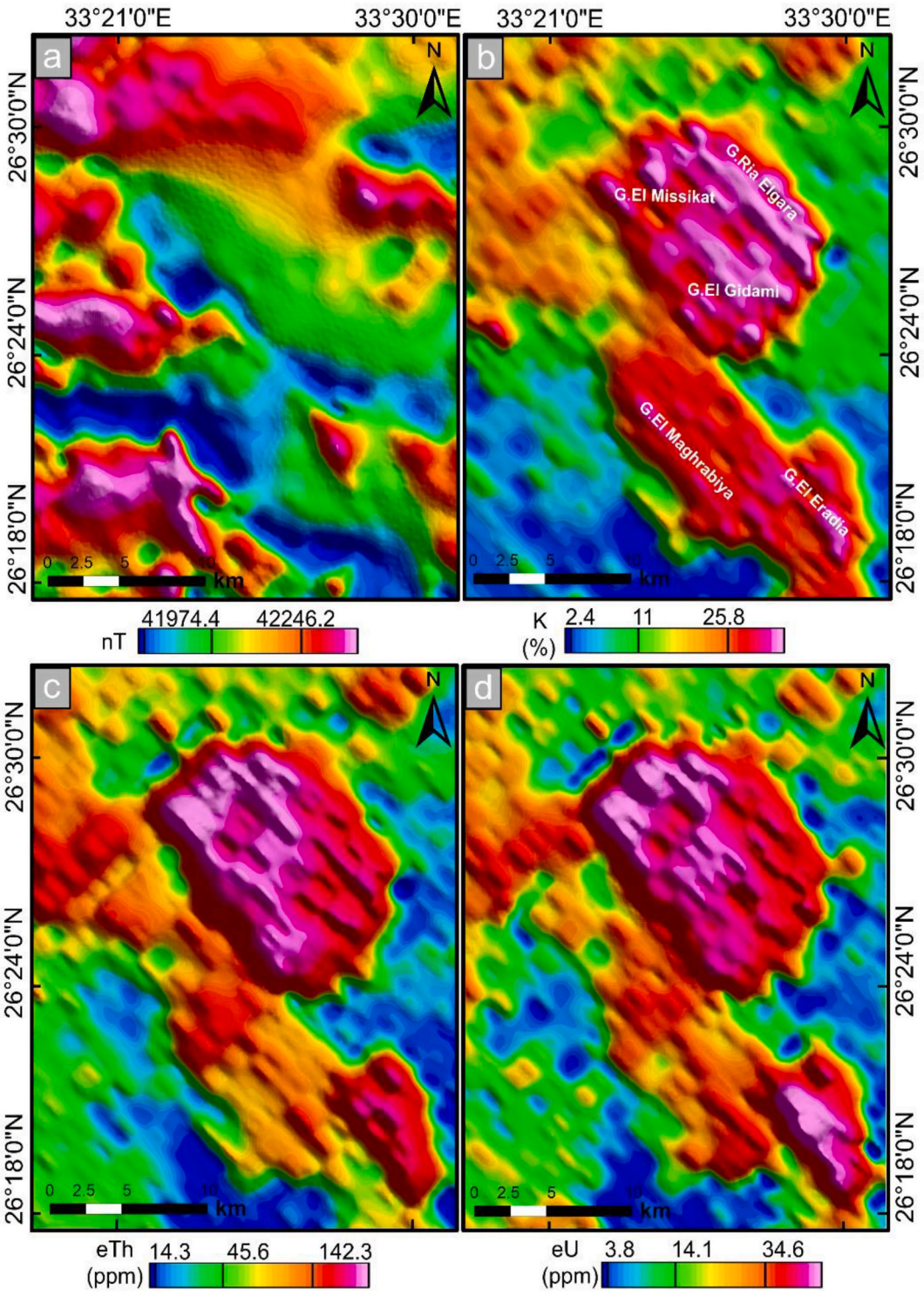


Fig. 8. (a) Total magnetic intensity map (TMI), spectrometric gamma-ray results: (b) potassium concentration (K), (c) equivalent thorium concentration (eTh) and (d) equivalent uranium concentration (eU).

4.2. Airborne geophysical data

The Reduced-to-Pole (RTP) data of the study area, as shown in Fig. 9a, is characterized by weak anomalies with some elongated high magnetic ones. The lowest magnetic values up to 41974.4 nT occupy the middle part of the area over G. El Missikat, G. El Gidami,

G. El Maghrabiya, G. El Eradia, while the highest magnetic anomalies with an amplitude of 42246.2 nT are placed in the western part. The high magnetic anomalies are noted to be oriented in NW and E-W directions. More structures (e.g., contacts, faults) are well defined in the TD map (Fig. 9b). The dashed white lines depicted on the TD map are oriented in NW, NE, N-S, and E-W. The NW direction is the most prominent one controlling the mineralization occurrences. The estimated depths of these structures from applying the Euler deconvolution approach of a contact model (Fig. 9c) reach 900 m, and most of the results fall between 0 and 300 revealing

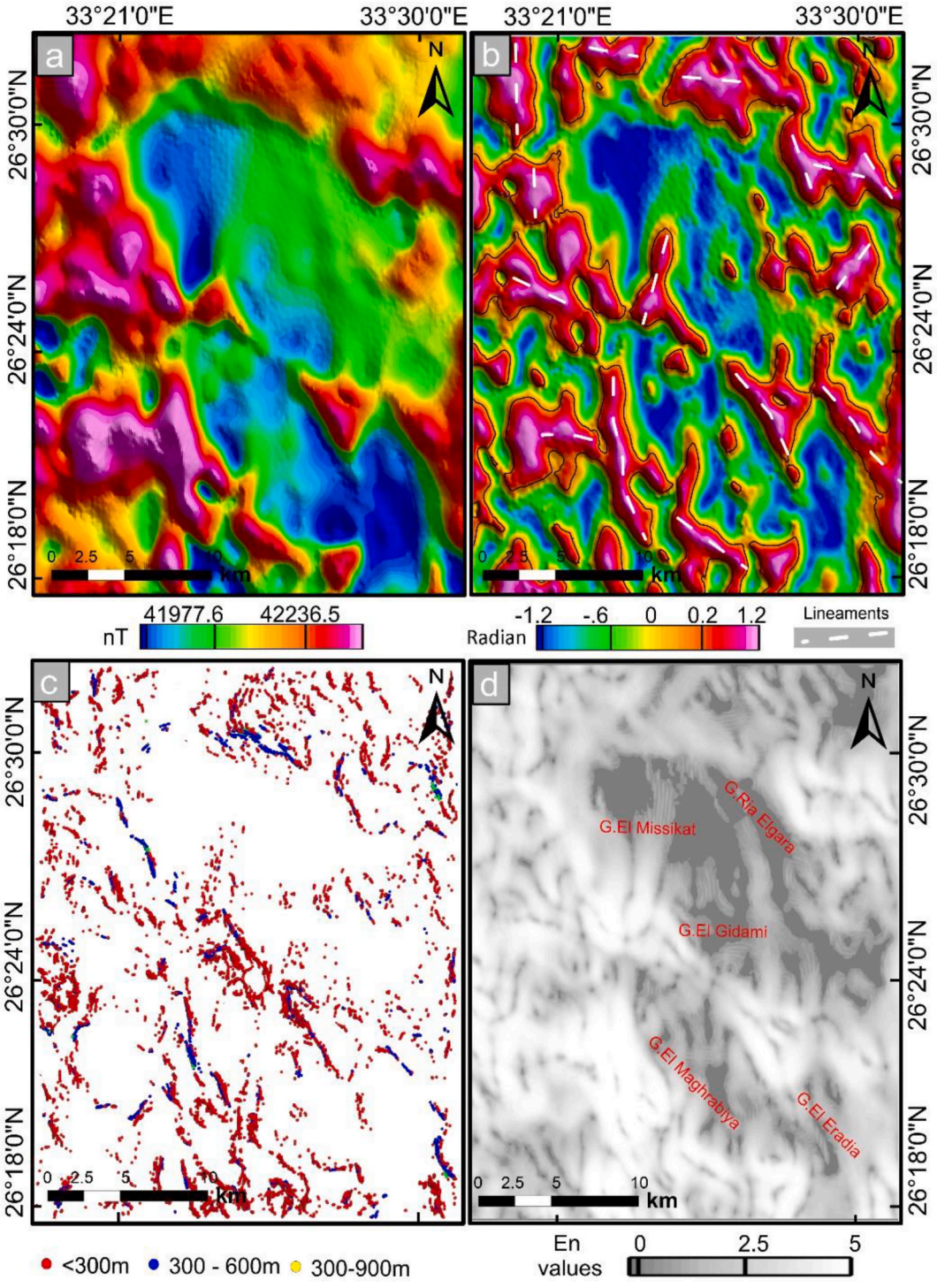


Fig. 9. (a) Reduction to pole maps (RTP), (b) TD map, (c) Euler solutions of contact model map (ED) and (d) Entropy map.

shallow sources. For automatically depicting lineaments that may control mineralization occurrence, a suite of CET grid analysis algorithms has been applied on RTP data, starting with generating an entropy map (Fig. 9d). The entropy measures the randomness of image and characterizes spread patterns of greyscale pixel magnetic intensities, improving the local magnetic causative sources, which

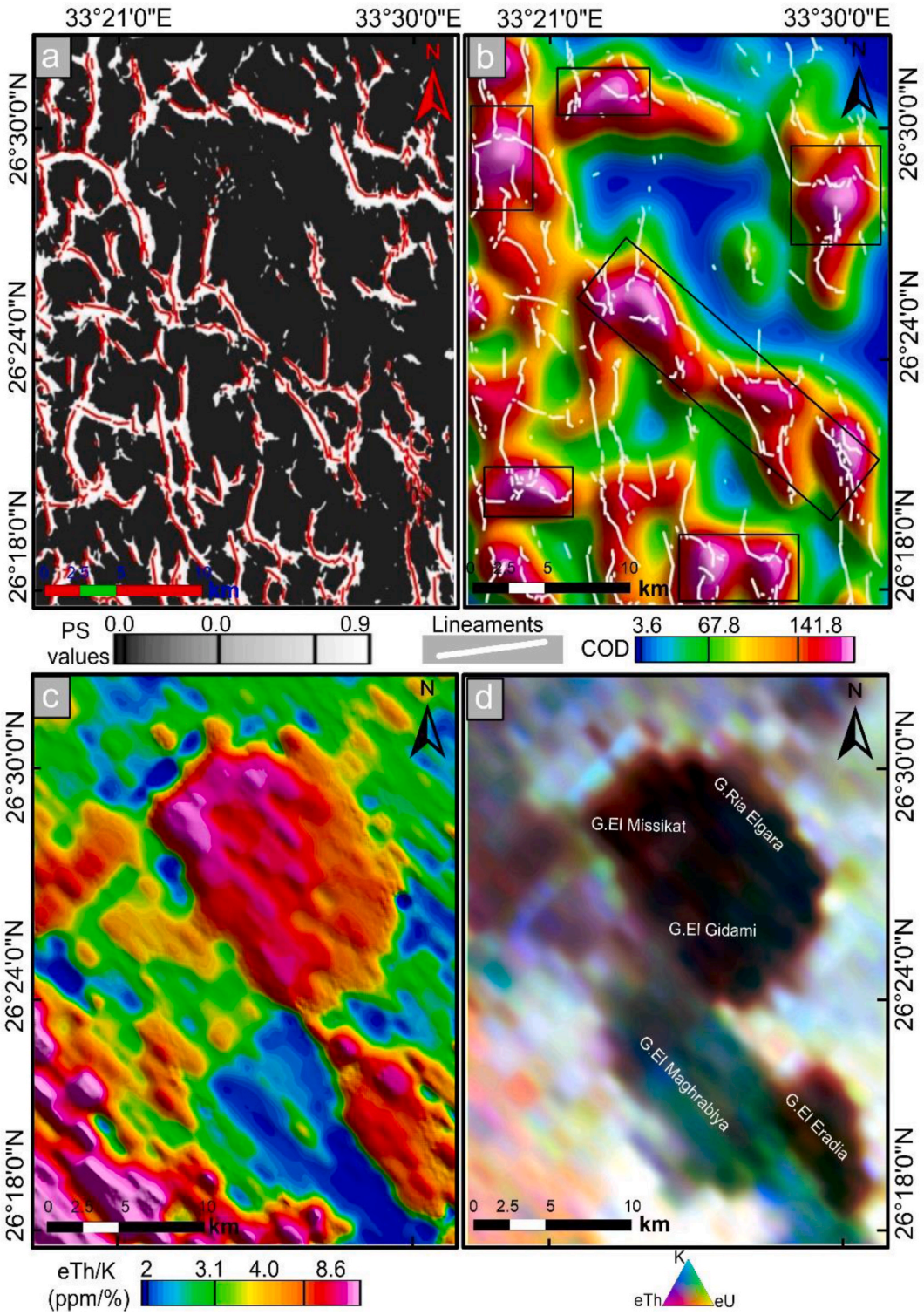


Fig. 10. (a) Phase symmetry map overlaid by thresholding skeletal features, (b) contact occurrence density heat map (COD), (c) eTh/k ratio map and (d) composite ternary map (CTM).

clearly are concentrated in the west-south part of the area and oriented in the NW direction. It is worth noting that the map diminished high-frequency noise and prevented delineating the edge of boundaries on both sides of a narrow anomaly. Afterward, the entropy map is utilized as input for phase symmetry (Fig. 10a) to map any laterally continuous line-like areas of discontinuity (distinguished by thick white colors and its a value is about 1), relying on the symmetry in the frequency components of the signal. The thick white line segments are reduced into skeletal features by applying thresholding (Fig. 10a) via non-maximal suppression, which suppresses the low values (black color) while retaining the high local maxima (thick white color). The output of thresholding is displayed as red color (Fig. 10a), which is then processed by skeletonization to generate axial lines. Finally, the skeletal lines are vectorized to produce a set of lineaments (straight line segments).

From the vectorization map (Fig. 10b) of the investigated area, we can note that most of the detected automated lineaments are oriented in the NW direction, which may control the mineralization occurrence in the area. Based on these results, a feature intersection density heat map (contact occurrence density) is generated and displayed in Fig. 10b. The favorable zones for the occurrence of valuable minerals are thought to be over the intersection of the lineaments, which is clearly expressed as a pink color on the map. These zones are concentrated in the west and southwest parts of the study area associated with aphanitic and plagioclase-phyric andesite-alkali granite. The altered parts of the area can be depicted by using eTh/K ratio map (Fig. 10c). Towards the discrimination between different rock units and highlighting high radioactive zones, a ternary composite map (Fig. 10d) was generated by modulating the three colors cyan for potassium concentration, magenta for thorium, yellow for uranium. The most lithological units mapped previously by remote sensing data are well defined using the ternary map. The most notable rock unit is the granite rock with black bands defining areas of high radioactive elements (K, eTh, and eU).

4.3. Field verification and petrographic investigation

4.3.1. Field verification

Integrating advanced technologies, including remote sensing data (PRISMA and Sentinel-2) and geophysical datasets (aeromagnetic surveys and airborne gamma-ray spectrometry), yielded pivotal and exceedingly satisfactory results. Fieldwork emerged as an indispensable factor in cementing the impressive results achieved, as it involved visits to numerous stations and meticulous sample collection from various locations across the study area (Fig. 11a–v). Fig. 11a–e illustrate the diverse lithological plutons within the area of study.

Samples from areas distant from shear zones revealed unaltered, non-mineralized granites, maintaining the pristine composition of the El-Erediya syenogranite pluton (Fig. 11f). In contrast, samples collected from the sheared and altered granite within the sheared area of Ria- El-Garra pluton and southern shear zone of the El-Erediya pluton showed significant alterations and notable radioactive mineralization (Fig. 11g–i). This unequivocally confirms that the shear zone hosts substantial alteration zones enriched with various mineral deposits, particularly radiological ones (Fig. 11j–l).

One of the predominant alteration processes of the study area is the silicification, characterized by quartz veins and repeated silica deposition (Shalaby et al., 2010) (Fig. 11m, n, and o). This alteration phenomenon holds considerable significance as it hosts numerous radioactive mineralizations (Fig. 11o). Several alteration zones have also been identified and confirmed within the shear zones, like hematitization, fluoritization, and kaolinization (Fig. 11p–s).

Dendritic formations of manganese oxides within shear zones associated with younger granitoid plutons serve as pivotal indicators of the influence of hydrothermal fluids. These hot aqueous solutions are instrumental for forming alteration zoned (Fig. 11t). The felsite veins located in the northeastern part of G. El-Missikat and the northern northern sector of G. El-Maghrabiya, stand out as some of the most significant geological features within the study area, renowned for their enrichment in radioactive mineralizations (Fig. 11u and v).

These profound observations, derived from extensive fieldwork, underscore the precision and effectiveness of our results achieved through advanced investigative techniques.

4.3.2. Petrographic investigations

To substantiate the assertion that the El-Missikat and El-Erediya areas experienced multiple episodes of hydrothermal activity, we can highlight the presence of extensive shear zones characterized by numerous fractures, joints, and faults. These geological features serve as conduits for the migration and circulation of hydrothermal fluids, resulting in mineral enrichment. The manifestation of hydrothermal alteration zones further supports this inference, as evidenced by distinct mineralogical changes in thin sections.

This comprehensive petrographic investigation aims to elucidate the geological processes at play and deepen our understanding of the mechanisms driving mineralization in the region. Furthermore, the presence of radioactive mineralization closely associated with hydrothermal alteration zones underscores the strong connection between hydrothermal activity and mineralization in the El-Missikat and El-Erediya areas.

El-Erediya granites, which predominantly consist of monzogranite and syenogranite, boast a rich mineral composition dominated by essential felsic minerals like quartz, K-feldspars (microcline and microcline perthites), and plagioclase (albite). Complementing these minerals, two fundamental mafic minerals, biotite and muscovite, occur. Additionally, secondary minerals such as sericite, epidote, kaolinite, and chlorite occur due to the alterations of the primary minerals. Beyond the essentials, accessory minerals add further complexity to the mineralogical composition through the presence of green to violet fluorite, monazite, allanite, zircon, apatite, and various opaques, including iron oxy-hydroxides and sulfides.

a. Rock-forming minerals

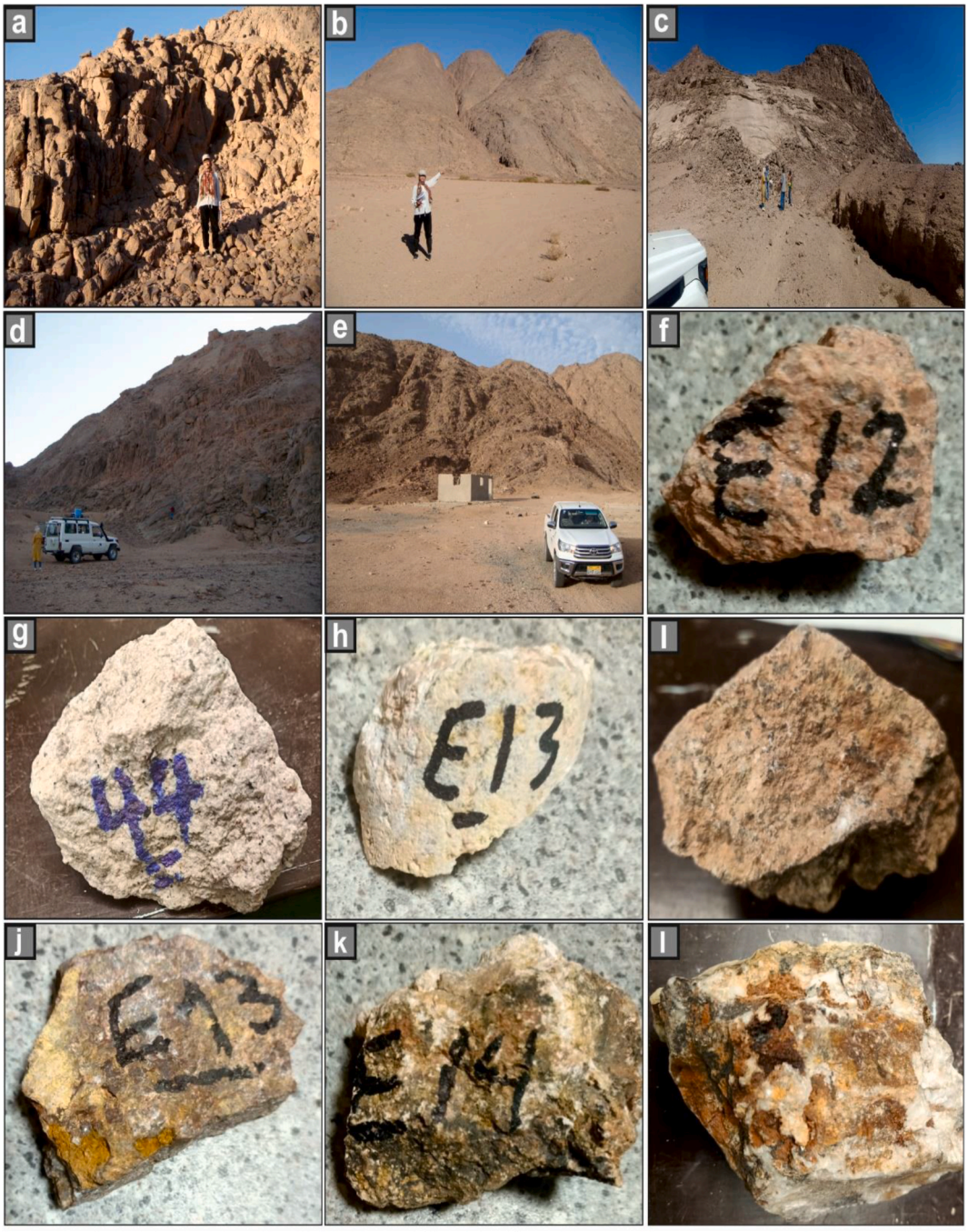


Fig. 11. (a) El-Missikat syenogranites pluton, (b) El-Gidami syenogranite plutons, (c) Ria El-Garaa syenogranite pluton (d) El-Maghrabiya monzogranite pluton (e) El-Erediya syenogranite pluton, (f) fresh syenogranite sample, (g) an albitized specimen meticulously retrieved from G. Ria El-Garaa, (h) U-mineralization bearing altered syenogranite sample, (i) hematitized specimen that pick out from the sheared zones, (j) U-mineralization bearing altered syenogranite sample extracted from the shear zone, (k) U-mineralizations bearing altered syenogranite samples retrieved from a mine proximal to the shear zone and (l) a mineralized black (smoky) silica vein specimen obtained from the shear zone within the El-Erediya syenogranite.
Fig. 11**:** (m, n) quartz veinlets traversing the syenogranite of El-Erediya, (o) red and black silica veinlets from the shear zone in northern sector of G. El-Missikat, (p, q) hematitization alteration zones prominently identified within the sheared zone in the northwestern sector of G. El-Missikat, (r) a highly fluoritized specimen obtained from the shear zone in the same northwestern sector of G. El-Missikat, (s) a kaolinization alteration zone indicative of advanced hydrothermal alteration processes, (t) dendritic-like forms of manganese mineralization within the younger granite pluton of El-Missikat due to post-magmatic hydrothermal fluid activity, (u) a felsite dyke intruding the older granitoids in NE part of El-Missikat pluton, with a

strike-slip fault cutting through this dyke and (v) felsite dykes intricately penetrate the younger granite in N- sector of G. El-Maghrabiya. **Symbols**: **FDY= felsite dyke, OG= older granite and YG= younger granite.**

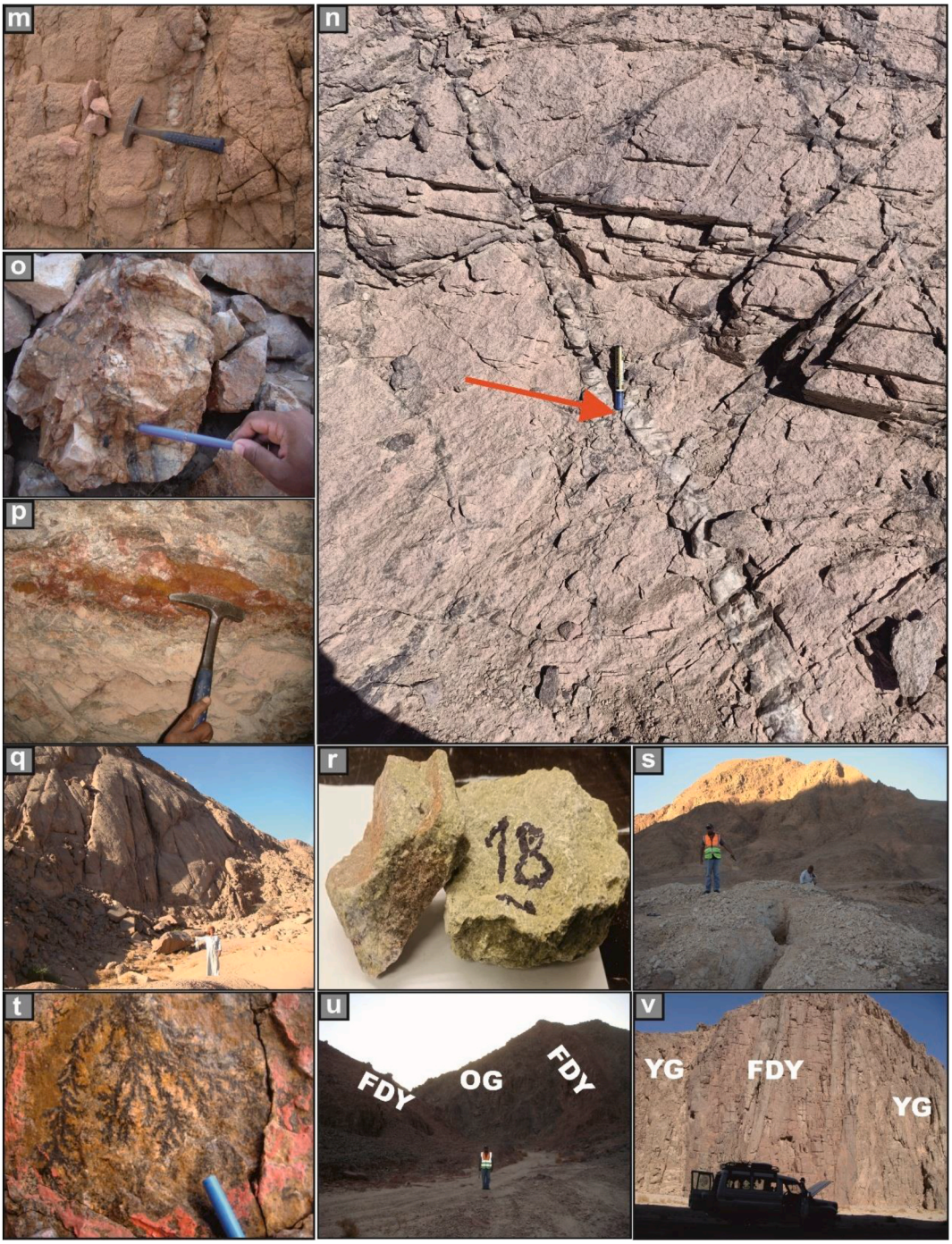


Fig. 11. (*continued*).

Quartz grains, roughly estimated to make up 30–35 % of the composition of the El-Erediya monzogranite, show anhedral to subhedral morphology. They demonstrate undulose extinction and contain abundant inclusions of apatite and zircon (Fig. 12a). **K-feldspar** grains, particularly perthite, comprising an estimated 31–34 % of the composition, similarly showcase anhedral to subhedral features. These grains frequently exhibit perthitic twinning and can often contain enclosed plagioclase and quartz crystals (Fig. 12a, b, and c). Occasionally, they undergo kaolinization or sericitization processes along shear zones. Additionally, they may include zircon inclusions (Fig. 12b). **Plagioclase** crystals assume prismatic shapes ranging from subhedral to euhedral. They frequently demonstrate

albite twinning and show evidence of sericitization and epidotization accompanied by the formation of secondary albite, especially on peripheries (Fig. 12c and d). **Biotite,** constituting approximately 1–2 % of the composition, appears as subhedral flakes with a color range spanning from yellowish-brown to dark brown, exhibiting pleochroism (dichroic). It sporadically contains minute inclusions such as long prismatic apatite, zircon, feldspar, quartz, and opaque minerals (Fig. 12e and f). Biotite occasionally undergoes partial alteration, resulting in the formation of chlorite.

Muscovite appears as irregular and intricately arranged fine to medium-sized flakes of primary or secondary origin after K-feldspar. It is colorless, commonly forms as an alteration product of K-feldspar, as evidenced by (El-Sherif, 2013), and is interwoven with quartz. It contains some elongated opaque spots, particularly along its cleavage (Fig. 12d and e). **Epidote** grains are typically euhedral in shape. They are usually colorless with shades of green (Fig. 12d and f). **Apatite** appears as elongated prismatic crystals and often exhibits a translucent to transparent appearance. Apatite crystals can vary widely in color depending on their chemical composition and any impurities present (Fig. 12g and h). **Zircon** occurs in euhedral to subhedral form and manifests in various shapes, ranging from short and elongated prismatic forms to bipyramidal shapes (Fig. 12b–d, and f). Their color spectrum encompasses hues such as pale yellow and colorless, sometimes from yellow to reddish-brown. Occasionally, zircon undergoes metamictization, a condition wherein the internal crystalline structure is disrupted by the bombardment of particles emitted by radionuclides (U and Th) within the crystal lattice (El-Kammar et al., 2021) (Fig. 12d and f). The metamictization of zircon gives strong evidence for the action of U-rich hydrothermal fluids in the study area.

The El-Erediya granite exhibits mineralization with several opaque sulfide minerals, such as pyrite, chalcopyrite, and sphalerite. **Pyrites** commonly display euhedral crystals with a brassy yellow hue and a cubic shape (Fig. 12c and d). **Iron oxides** emerge as the most abundant and widely distributed among minerals, manifesting as subhedral crystals exhibiting a subdued red hue (Fig. 12c and e).

b. Alteration mineralogy

The petrographic description of these samples provides crucial insights into the mineralization processes resulting from hydrothermal solutions. In addition, radioactive mineralizations (U-mineralization) are closely linked to different alteration processes.

Silicification emerges as the primary alteration process within the shear zone, driven by magmatic-hydrothermal solutions. This phenomenon unfolds in distinct pulses, resulting in the generation of a diverse variety of quartz veins exhibiting varying colors (milky quartz, black smoky quartz, and red jasper) and characteristics (Abd El-Naby, 2008; Abdel-Hakeem et al., 2023; El-Kammar et al., 2021; El-Leil et al., 2015). During the silicification process, secondary quartz appears in fine crystals or forms amorphous silica in the interstitial spaces between the original magmatic quartz grains and feldspars, or fills fractures and voids in the shear zone. Notably, secondary uranium minerals such as uranophane and autunite, as well as other radioactive element-bearing minerals such as thorite can be observed in association with this type of alteration, and are sometimes embedded in secondary quartz in the shear zone and are often stained with iron oxides, like hematite (S1 a, b, and c).

Kaolinitization (argillic alteration) is characterized by the development of kaolinite along the fissures and fracture planes in the shear zones. This alteration arises from the deep hydration of K-feldspar, especially perthite, due to acidic solutions at relatively low temperatures, typically between 200 and 280 °C (Abu-Deif and El-Tahir, 2008; El-Kammar et al., 2021), according to the following equation. This unique alteration phenomenon can absorb uranium minerals within shear zones. As a result, small veinlets containing uranophane are frequently found alongside kaolinite, often exhibiting staining from iron oxides (hematite) (S1 d, e, and f).

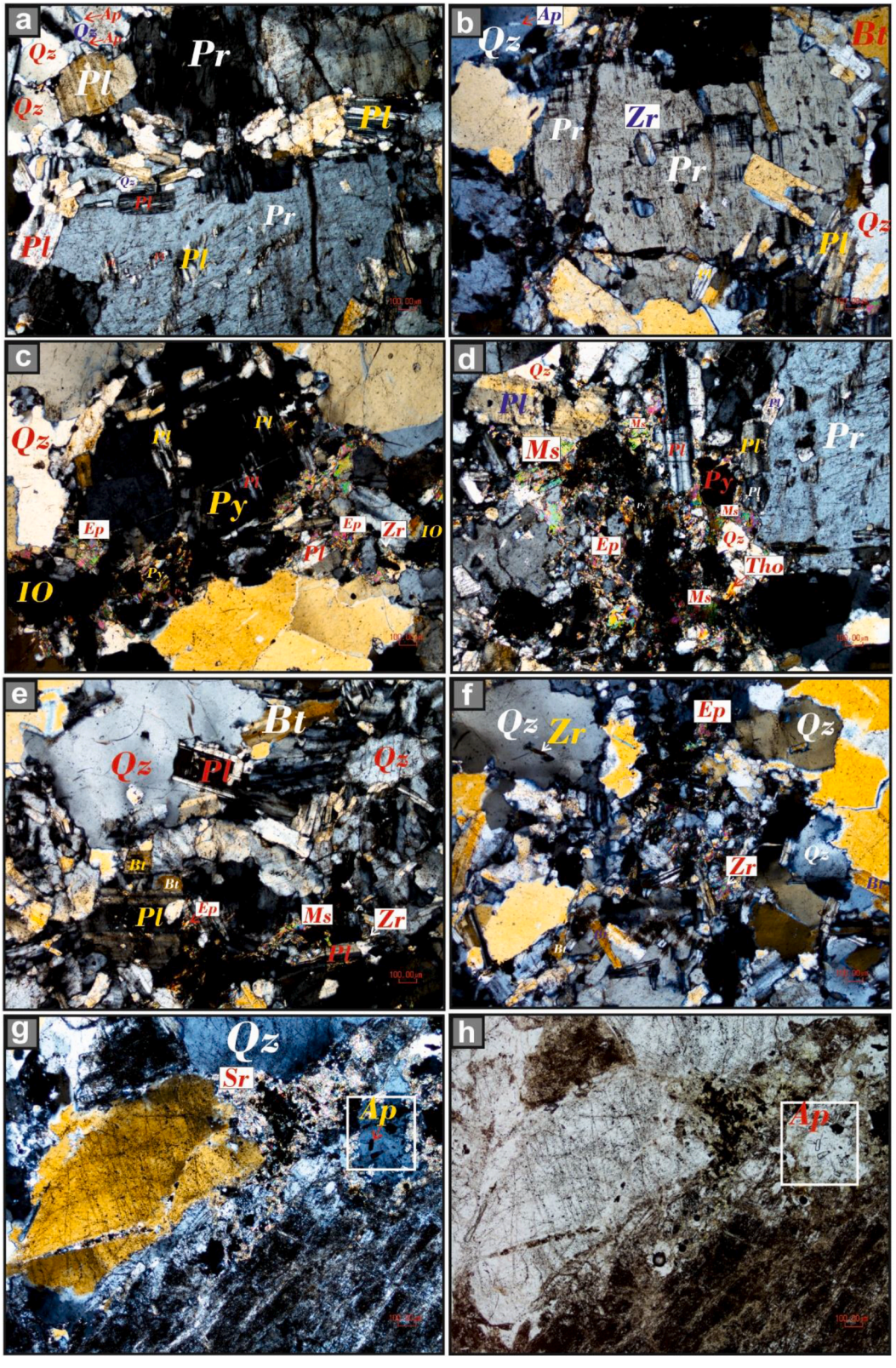
$$KAlSi_3O_8 + 2H_2O \rightarrow Al_2Si_2O_5(OH)_4 + K + Si(OH)_4$$

Hematitization or Ferrugination, iron oxide-bearing hydrothermal solutions, predominantly hematite, goethite, and limonite, demonstrate a pronounced tendency to permeate the original mineral composition of granite rocks, instigating a staining process for these minerals. These iron oxides are produced due to the oxidation and weathering of primary magnetite and pyrite within shear zones (Abdel-Hakeem et al., 2023; Abu-Deif and El-Tahir, 2008; Hassaan et al., 2022). This infiltration not only initiates a transformation in the rock's appearance but also fosters a closer interaction between iron oxides and uranium minerals, which enables the concurrent presence of uranium minerals (pitchblende, uranophane, kasolite, and autunite) alongside iron oxides within the framework of the original rock mineralogy. This alteration type associated with silicification along the shear zone manifests a higher radioactivity level than the sericitization and kaolinization (S1 g, h, and i).

Sericitization (phyllic alteration) represents the destabilization of feldspars in the presence of H^+, OH, K, and S, resulting in the formation of sericite (Shahin et al., 2021). This phenomenon consistently accompanies hematitization and kaolinization processes, forming an interconnected network of hydrothermal alteration products within the shear zones. Additionally, sericitization is frequently associated with secondary uranium mineralizations, suggesting a complex interplay between mineral alteration processes and the potential for mineral enrichment in these zones (S1 j and k).

Epidotization (propylitic alteration) refers to the process by which minerals, typically primary silicate minerals such as feldspars (plagioclase), are altered into epidote through hydrothermal processes (Meyer, 1967). In this context, we observe that the morphology of some epidote grains adopts a fan-like shape due to their association with and proximity to secondary uranium minerals (S1 l and m).

Albitization (propylitic alteration) of plagioclase entails removing its anorthite content via decalcification, often accompanied by saussuritization (El-Kammar et al., 2021). This process is driven by the interaction of high-temperature alkaline hydrothermal solutions with early-formed feldspars within granite, enriching and forming albite clots. These clots corrode and replace previously formed K-feldspar (perthite) and quartz along various mineralogical features, such as cleavage, twinning planes, and grain boundaries (S1 n



(caption on next page)

Fig. 12. Cross polarized (XPL) and plane polarized (PPL) photomicrographs showing (a, b) syenogranite, showing a hypidiomorphic texture, (c, d) high alteration of plagioclase to epidote and distribution of pyrite mineralizations, (e, f) metamictization of zircon crystals and (g, h) elongated prisms of apatite crystals enclosed in feldspars. **Symbols**: **Qz** = quartz, **Pl** = plagioclase, **Pr** = perthite, **Ap** = apatite, **Zr** = zircon, **IO** = iron oxides, **Bt** = biotite, **Py** = pyrite, **Ep** = epidote, **Ms** = muscovite, **Tho** = thorite, and **Sr** = sericite.

and o).

$$CaAlSi_2O_8 + 2Na^+ + 4SiO_2 + 2H^+ \rightarrow 2NaAlSi_3O_8 + Ca_2^+ + H_2O$$

c. Uranium Mineralization

Indeed, as gleaned from the sample descriptions, uranium mineralization is prominently distributed along fissures, joints, and shear zones, particularly those undergoing hydrothermal alteration. Uranium minerals, including uraninite or pitchblende, are recognized as primary uranium minerals. Complementing these are secondary uranium minerals, like uranophane, kasolite, and autunite, which are abundant in areas of intense alteration. Additionally, accessory minerals such as zircon and thorite host radioactive elements (S1 and Apx 1).

4.3.3. Scanning electron microscopy with energy dispersive X-ray spectroscopy (SEM-EDX)

The SEM-EDX analysis results of the samples collected far from the shear zones have confirmed the presence of accessory minerals. These minerals were previously identified in the El-Erediya granite through prior studies (Abd El-Naby, 2008; Abdel-Hakeem et al., 2023; Amer, O., Kharbish, S., Maged, A., and Khedr, 2021; El-Kammar et al., 2021; Hassaan et al., 2022).

Fluorite, zircon, thorite, columbite, monazite, and cassiterite were verified to be present. Furthermore, the study area yielded the discovery of previously unidentified minerals, such as polycrase-Y and plumbopyrochlore or (Pb-pyrochlore) (S2 and Apx 2).

Furthermore, based on the SEM analysis conducted on the samples proximate to the shear zones and bordering the alteration zone, it was confirmed that these samples contain radioactive mineralization. These minerals are linked with other mineralizations observed in the alteration zones and exhibit a significant concentration of radioactive elements associated with rare metal mineralization, mirroring the composition found within the alteration zones. This observation corroborates findings documented in previous studies (Abd El-Naby, 2008; El-Kammar et al., 2021; El Mezayen et al., 2017; Raslan, 2009).

Specifically, uraninite (pitchblende), uranothorite, columbite, rutile, and zirconolite have been conclusively confirmed. The latter mineral is regarded as one of the newly discovered minerals within the study area, previously unmentioned in any preceding studies (S2 and Apx 2).

4.3.4. Elemental mapping using SEM-EDX

SEM-EDX facilitates the observation of spatial element distribution within a sample, which is particularly crucial for analyzing the distribution of elements, especially radioactive ones, within the sample. This capability is vital for identifying the most common elements present and understanding their spatial arrangement. In this investigation, special emphasis was placed on the samples extracted from the shear zones.

A thorough analysis of elemental maps was conducted to visualize the spatial distribution of elements within parts of the samples, which are referred to as elemental maps 1, 2, and 3 (S3). These maps provided insights into the distribution patterns of crucial elements such as uranium (U), niobium (Nb), iron (Fe), and silicon (Si) throughout the samples. They resulted in deeper insights into the complex interplay between uranium elements and various others.

The uranium typically embodied in minerals such as uraninite or pitchblende (S3 c, I, and o) exhibits a notable interconnection with niobium, which refers to columbite mineralization (S3 d, j, and p). Moreover, iron elements, primarily manifested through iron oxides, which hold pivotal significance in alteration zones, are often associated with uranium elements in the majority of the samples (S3 e, k, and q). These intricate associations are vividly illustrated in Supplementary 2l (S2 l) and the three elemental maps. Additionally, the detection of silica elements associated with uranium underscores the ongoing silicification process within alteration zones situated amidst shear zones (S3 f, l, and r).

In essence, the amalgamation of these findings substantiates the proposition that uranium mineralization observed within shear zones is intricately entwined with the alteration zones and the mineralization phenomena occurring therein. This has been proven based on our comprehensive microscopic examination and SEM-EDX analysis.

5. Discussion

El-Missikat and El-Erediya granites stand as one of the most pivotal uranium reservoirs in Egypt, possessing extraordinary potential for bolstering the national economy. Despite numerous previous investigations (Abd El-Naby, 2008; Amer, O., Kharbish, S., Maged, A., and Khedr, 2021; El-Leil et al., 2015; El Mezayen et al., 2017; Elsaid et al., 2014), these granitoids remain insufficiently explored, necessitating the application of more sophisticated and precise research methodologies. Previous research has provided an invaluable foundation, offering insights into existing findings while highlighting areas that require further exploration. Numerous previous studies have extensively examined the area of study, focusing on lithology, geological structures, and mineralization in alteration zones, utilizing ASTER, Landsat ETM, and Landsat 8 imagery. Additionally, Radiological assessments, using ground-based surveys.

Each prior study was guided by distinct objectives, but all their overarching ambitions invariably focused on radioactive mineralization deposits.

The objective of our study was equally significant to that of previous research, it focuses on the exploration of radioactive minerals. But our approach was distinctly characterized by an unwavering commitment to precision and methodological efficiency. As exploration and identification of uranium ore deposits are not only beneficial to society's economic development, but also contribute to local environmental protection, especially for groundwater pollution. So we integrate high-resolution satellite imagery (Sentinel-2 and PRISMA) with airborne geophysical data (magnetic and radiometric) for highly accurate assessment of the spatial distribution of radioactive mineralization in El-Missikat and El-Erediya regions.

Relying on the robust evidence derived from these cutting-edge methods and tools is vital to validate previous findings and guarantee the precision and trustworthiness of the outcomes to identify unexplored regions that were not the focus of prior investigations. This approach strengthens the credibility of research and establishes the hybrid method as a dependable resource for future geological studies.

Radioactive mineralizations, particularly uranium mineralization within the study area, are intrinsically associated with the younger granitic formations. These mineralizations are predominantly concentrated within shear zones, where an extensive network of fractures and faults facilitates the movement of mineralization-laden hydrothermal solutions. As these fluids traverse the fractured rock matrix, they deposit mineral concentrations, forming distinct alteration zones. These alteration zones serve as crucial indicators, marking the loci of radioactive mineralizations and reflecting the dynamic interplay of geological processes responsible for their formation.

Undoubtedly, the integration of advanced remote sensing technologies with geophysical datasets, particularly airborne gamma-ray spectrometry, has played a pivotal role in the precise mapping of high radioactive zones and differentiation of various rock types distributed across the study area. This was effectively achieved through the application of MNF 8, PC2, IC9, and PC4 techniques on PRISMA satellite imagery (Fig. 3a–d), alongside the utilization of a ternary composite map (Fig. 10d), demonstrating the synergy of these modern methodologies in lithological mapping. The controversy surrounding the amphibolite rocks, which are integral components of the ophiolite group, was a focal point in the lithological mapping of the study area across numerous prior studies. Divergent opinions emerged, with some asserting their presence (El Mezayen et al., 2017; Abd El-Naby, 2008) and others refuting it (Elsaid et al., 2014; Kassas and Bakhit, 1989). However, this challenge was effectively addressed through the application of the hybrid methodology, which provided a comprehensive resolution (Figs. 3b and 10d). Further exploration within the study area, as each collection of syn-tectonic older granites (Abd El-Naby, 2008; El-Leil et al., 2015; Elsaid et al., 2014) and post-tectonic younger granites (Abd El-Naby, 2008; Bakhit and Kassas, 1989; El Mezayen et al., 2017; Elsaid et al., 2014; Kassas and Bakhit, 1989) contains specific types. The hybrid experiment successfully generated a conclusive framework, delineating a definitive map to segregate the two species with precision and enabling an unambiguous distinction between them (Figs. 3c and 10d). This technologies facilitated also the generation of exceptionally precise and detailed mapping of the younger granitic plutons (our target) for the study area (Fig. 3d), using PC4 on PRISMA satellite images. This result was strengthened especially, when a composite ternary map (CTM), has been applied (Fig. 10d). For the first time in the studied area, the combination provided a robust framework and delineation of the younger granitic formations was meticulously confirmed with exceptional precision, culminating in the resolution of the mapping process for these rocks. As previously highlighted, these findings align closely with those established in earlier studies, reinforcing our confidence in the advanced hybrid methodologies.

The application of the hybrid methodology extended beyond mere geological mapping, proving instrumental in uncovering robust indicators of radioactive mineralization. This approach facilitated the precise identification of shear zones intimately associated with the younger granites, which play a critical role in governing the distribution of radioactive mineralization. These shear zones were delineated in key areas, including the N and NW regions of G. El-Missikat, the N and NW sections of G. El-Maghrabiya, and the S portion of G. El-Erediya (Fig. 4a), by using MNF6 on PRISMA satellite images. These findings were substantiated, with the optimal locations for the manifestation of radioactive mineralization being precisely delineated through the generation of a heatmap illustrating density distribution (contact occurrence density) (Fig. 10b). These zones are seen to be associated with the alkali granite, specifically in the sheared zone. Fluorite is among the prominent minerals discovered within shear zones, consistently occurring alongside uranium mineralizations. Remote sensing techniques have been instrumental in enabling us to precisely pinpoint the target areas through the application of PC2 on PRISMA satellite images (Fig. 4b). Prolonged exposure of the syenogranites within the study area to hydration and weathering processes has culminated in pronounced K-metasomatic alteration. By employing our advanced hybrid methodologies, we unequivocally confirmed the presence and extent of this alteration, as the radiometric K/eTh ratio helped us to clearly detect areas of potassic alteration (Fig. 4c and 10c). Extensive research has consistently validated the occurrence of diverse mineralization deposits, specifically Greisenization. This phenomenon arises from granitic intrusions and occurs as a result of fractional crystallization, driven by the interaction of residual Sn-rich fluids that segregate from the crystallizing magma (Ridley, 2013). Our innovative hybrid methodology (IC6 with density heat map) has proven highly efficacious in definitively substantiating the presence of these mineralizations near intrusion zones with remarkable precision and reliability (Fig. 4d and 10b).

The hybrid methodology proved instrumental and pivotal in the precise identification of alteration zones within shear zones that host radioactive mineralization. Moreover, it provided the opportunity to uncover previously unexamined alteration zones, hoping to find the potential for the presence of radioactive deposits. The alteration zones within shear zones were well-documented for hosting significant uranium mineralizations (Abd El-Naby, 2008; Abdel-Hakeem et al., 2023; Ammar et al., 2016; El-Leil et al., 2015). The study area exhibits three main alteration types: argillic (illitization and kaolinization), phyllic (silicification, sericitization and carbonatization), and propylitic (chloritization, albitization, epidotization, fluoritization and hematization) (El-Sherif, 2013; Hassaan et al., 2022; Abu-Deif and El-Tahir, 2008; Ammar et al., 2016; El-Kammar et al., 2021; El Mezayen et al., 2017; Elsaid et al., 2014;

Hussein et al., 1986). In this study, applying the Sabin technique on Sentinel-2 imagery was the most successful, as we highlighted the dominant alteration types (hematization and manganese alterations, kaolinization and sericitization) in these sheared areas (Fig. 5a, b, and d). These results were substantiated, and the precise coordinates of the alteration zones were delineated through the application of the K/eTh ratio obtained from airborne radiometric measurement, that was good in determine and confirm the k-alteration (sericitization) (Fig. 10c). Although the term "gossan" may not have been widely recognized within the study area, the phenomenon it describes aligns closely with the observed geological processes. Gossans, weathered rock formations atop sulfide-rich mineral deposits like pyrite or chalcopyrite, exhibit a reddish-brown hue due to the oxidation of sulfides upon exposure to air and water into iron oxides (hematite, goethite). This process, mirroring gossan formation mechanisms, aligns with previous findings, as has been noted the presence of pyrite accompanied by repeated silica generation within the shear zones, followed by pyrite oxidation (Abd El-Naby, 2008; Abu-Deif and El-Tahir, 2008; Ammar et al., 2016; El-Kammar et al., 1997, 2021; Hassaan et al., 2022). Notably, gossan-rich zones often overlap with iron ore deposits, though not exclusively. Our advanced hybrid methodology, when applied to Sentinel-2 imagery alongside the Total Magnetic Intensity map, effectively corroborated and pinpointed the presence of gossan with exceptional precision, demonstrating its efficacy in detecting such mineralogical features (Fig. 5c and 8a)

Towards to the linear structural features within the study area, we have noticed that, in the NE boundary of the El-Missikat granitic pluton, there are NE-SW trending felsite dyke swarms traversing the area. These dykes cut through older granitoids but do not extend into the younger granites (El-Kammar et al., 2021). In addition, in the NW section of El-Missikat, the younger granite pluton is intruded by NE-SW striking aplite and lamprophyric dike swarms (~1.5 m thick) (El-Leil et al., 2015). These intrusions observed at the main adit of the mine located in the NE part of G. El-Missikat resulted in triggering shearing, mylonitization, and alterations such as brecciation, silicification, and kaolinization (El-Leil et al., 2015). These dykes have been meticulously delineated using advanced remote sensing techniques, including Sentinel-2 and PRISMA imagery (Fig. 6a–d), and their presence has been unequivocally validated through geophysical analysis, as evidenced by the vectorization map (Fig. 10a), demonstrating the precision and efficacy of the hybrid methodology.

The structural lineaments governing the distribution of radioactive mineralizations within the study area were unequivocally validated. These lineaments facilitated the precise localization of radioactive mineral deposits while significantly reducing the margin of false probabilities, thereby enhancing the accuracy of the findings. A suite of filters, including TD, ED, and CET grid analysis algorithms, has already been applied to the RTP data. From the vectorization map (Fig. 10a), we noted that most of the detected automated lineaments controlling the mineralizations are oriented in the NW direction. This observation aligns seamlessly with our earlier findings, wherein shear and alteration zones are extensively prevalent throughout the northern and southwestern regions of the granitoid plutons. These results also align with major fault orientations in the study area (Fig. 7).

The hybrid methodology proved highly efficacious in minimizing effort, time, and financial expenditure. Leveraging multiple lines of evidence to corroborate and improve exploration of radioactive mineralization (uranium) is inherently more reliable than relying on a single source. While remote sensing data is invaluable, it is not infallible and may, albeit rarely, yield occasional inaccuracies. Even for the same sensor, multi-temporal data could result in various anomalies (Hu et al., 2018), therefore, a combination of two optical sensors is strongly recommended for further geological investigations to obtain focused real anomalies. Consequently, supplementary techniques, such as geophysical data analysis, were employed to bridge any minor gaps that may arise from remote sensing methodologies, while simultaneously validating the results to ensure greater accuracy and reliability. Conducting fieldwork and engaging in on-ground investigations represented the most pivotal and conclusive step in validating the efficacy of this hybrid methodology. Ultimately, these integrative and robust methodologies facilitated the precise detection and delineation of high-anomaly zones harboring uranium deposits. It was definitely ascertained that radioactive minerals are inherently linked to alteration zones within the shear zones that intersect the younger granitic formations. It also excelled in identifying the predominant trend of radioactive mineralization, a task that proved challenging to achieve using individual methods alone. Its integration was indispensable to ensure both accuracy and precision in the results. Our research culminated in the development of a comprehensive map that synthesizes all employed methodologies, effectively delineating potential areas in radioactive mineralizations (Fig. 13).

6. Conclusions

For the first time over the study area, this study adopts integrated Sentinel-2, PRISMA) and advanced airborne geophysical techniques, including magnetic and radiological surveys, to enhance precision and efficiency in precise differentiation of rock formations, identification of shear zones, and mapping of alteration zones that harbor radioactive mineralization.

Leveraging PRISMA hyperspectral imagery alongside the ternary composite maps enabled the precise mapping and delineation of younger granitic formations within the study area with exceptional accuracy. This approach also facilitated the identification of shear zones closely associated with these granites, which play a pivotal role in controlling the distribution of radioactive mineralization. Employing the Sabin technique on Sentinel-2 imagery and the K/eTh ratio derived from airborne radiometric data successfully delineated hematization, manganese alterations, kaolinization, and sericitization. Furthermore, the structural lineaments controlling the spatial distribution of radioactive mineralizations were unequivocally delineated, where they oriented in the NW direction, aligning consistently with the orientations of major faults within the region, as well as the shear zones.

Rigorous field studies and microscopic analyses, including SEM-EDX, validated our findings, confirming the integration of remote sensing and geophysical data in identifying diverse alteration zones associated with radioactive mineralization. These investigations revealed the intricate relationship between radioactive mineralizations (U-mineralization) and alteration zones, especially silicification, kaolinitization, ferrugination, sericitization, epidotization, and albitization, that we mapped during our study. Thus, the adopted methodology is recommended to be followed for radioactive mineralization investigations.

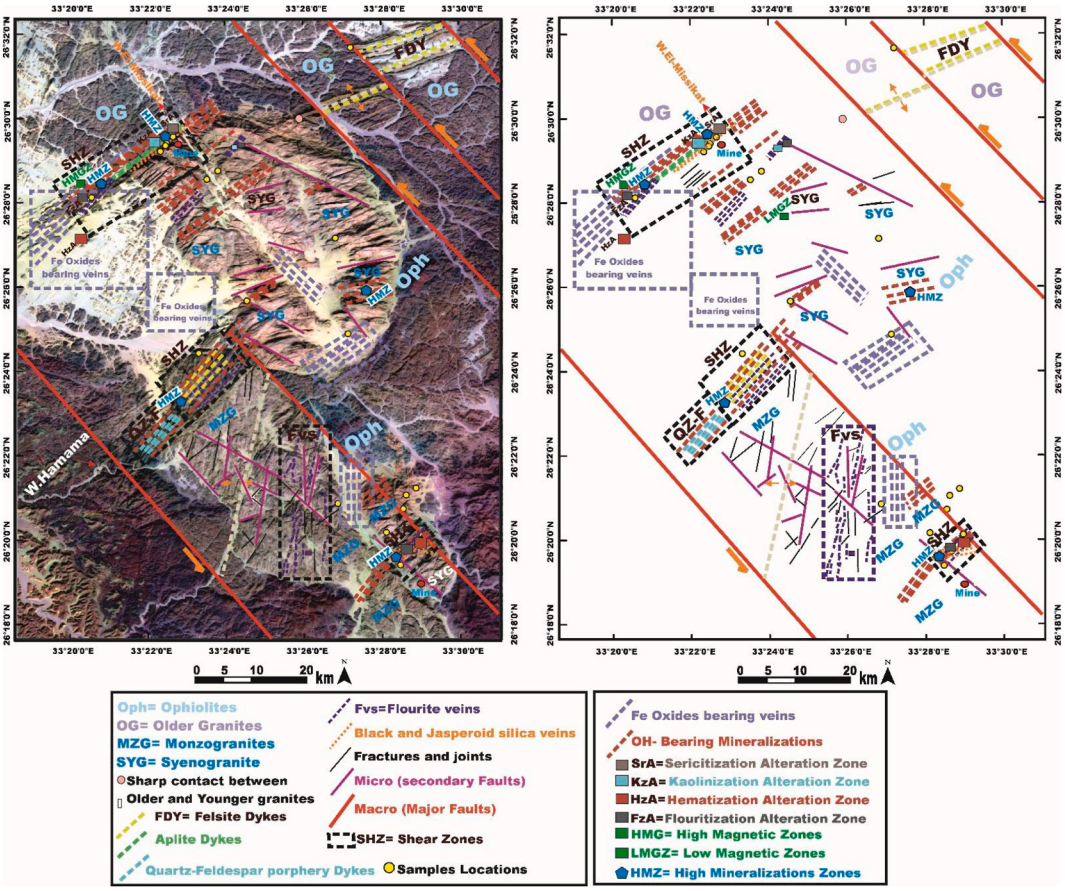


Fig. 13. The potential map shows areas of high radioactive mineralization (uranium anomaly) in the study area.

CRediT authorship contribution statement

Aya S. Shereif: Writing – original draft, Methodology. **Ali Shebl:** Writing – review & editing, Methodology. **Mahmoud Abdellatif:** Writing – review & editing, Methodology. **Mohamed A. Abdelkader:** Writing – review & editing, Methodology. **Mohamed Badawi:** Writing – review & editing, Methodology. **Abdelhalim S. Mahmoud:** Writing – review & editing, Methodology. **Árpád Csámer:** Writing – review & editing, Supervision.

Ethical statement

The preparation of this manuscript needs no ethical consideration more than the necessary references.

Declaration of competing interest

The authors declare that they have no known competing financial interests or personal relationships that could have appeared to influence the work reported in this paper.

Acknowledgments

This study is part of the first author's PhD research at the University of Debrecen. Aya S. Shereif is funded by the Stipendium Hungaricum Scholarship under the joint executive program between Hungary and Egypt. Many thanks to the University of Debrecen for the great support. The authors wish to extend their sincere gratitude to all individuals who provided valuable assistance and support during the fieldwork.

Appendix A. Supplementary data

Supplementary data to this article can be found online at https://doi.org/10.1016/j.rsase.2025.101624.

Data availability

No data was used for the research described in the article.

References

Abd El-Naby, H.H., 2008. Genesis of secondary uranium minerals associated with jasperoid veins, El Erediya area, Eastern Desert, Egypt. Miner. Depos. 43, 933–944.

Abdel-Hakeem, M., El-Tahir, M., Zeid, E.A., Rageh, H., 2023. Genetic implications of Th/U, Th/K, and U/K ratios for U mineralizations: a case study from El-Missikat and El-Erediya shear zones, Eastern Desert, Egypt. Geochem. Trans. 24, 3.

Abdelkareem, M., Akrby, A., Fakhry, M., Mostafa, M., 2018. Using of remote sensing and aeromagnetic data for predicting potential areas of hydrothermal mineral deposits in the central eastern desert of Egypt. Remote Sens. 7, 1.

Abu-Deif, A., Ammar, S.E., Mohamed, N.A., 1997. Geological and Geochemical Studies of Black Silica at El-Missikat Pluton, Central Eastern Desert, Egypt. Proc. Egypt. Acad. Sci., pp. 335–346

Abu-Deif, A.A., El-Tahir, M.A., 2008. A new uranium occurrence, Gabal El-Missikat prospect, central eastern desert, Egypt. Earth Sci. 19.

Aero-Service, 1984. Final operational report of airborne magnetic/radiation survey in the Eastern Desert, Egypt. For the Egyptian General Petroleum Corporation (EGPC) and the Egyptian Geological Survey and Mining Authority (EGSMA).

Amer, O., Kharbish, S., Maged, A., Khedr, F., 2021. Geochemical insight into granite hosted U-rich fluorite, Gabal El-Erediya area, Central Eastern Desert, Egypt: REE geochemical and fluid inclusion aspects. Arabian J. Geosci. 14, 1–17.

Ammar, F.A., Omar, S.A.M., El Sawey, E.L.S.H., 2016. Genetic affiliation of gold and uranium mineralization in El-Missikat granite, Central Eastern Desert, Egypt. Nucl. Sci. Sci. J. 5, 33–47.

Assiri, A.M., 2016. Remote Sensing Applications for Carbonatite Assessment and Mapping Using VNIR and SWIR Bands at Aluyaynah. UA E. Michigan State University.

Bakhit, F.S., Kassas, I.A. El, 1989. Distribution and orientation of radioactive veins in the El erediya-el missikat area, central Eastern Desert, Egypt. Int. J. Remote Sens. 10, 565–581.

Bentahar, I., Raji, M., 2021. Comparison of Landsat OLI, ASTER, and Sentinel 2A data in lithological mapping: a case study of rich area (Central High Atlas, Morocco). Adv. Space Res. 67, 945–963.

Campbell, J.B., Wynne, R.H., 2011. Introduction to Remote Sensing. Guilford Press.

Clark, R.N., 1999. Spectroscopy of rocks and minerals, and principles of spectroscopy. In: Rencz, A. (Ed.), Manual of Remote Sensing, vol. 3. Wiley and Sons Inc., New York. NY, USA, pp. 3–58.

Crippen, R.E., Blom, R.G., Heyada, J.R., 1988. Directed band ratioing for the retention of perceptually-independent topographic expression in chromaticity-enhanced imagery. Remote Sens. 9, 749–765.

Crosta, A.P., De Souza Filho, C.R., Azevedo, F., Brodie, C., 2003. Targeting key alteration minerals in epithermal deposits in Patagonia, Argentina, using ASTER imagery and principal component analysis. Int. J. Remote Sens. 24, 4233–4240.

Darenely, A.G., Ford, K.L., 1989. Regional airborne gamma-ray survey: a review. In: Proc. 3rd Inter. Conf. Geophys. Geochem. Expl. For Minerals and Ground Water, Ontario. Geol. Surv. Spec., pp. 229–240

Dawood, Y.H., Abd El-Naby, H.H., 2001. Mineralogy and genesis of secondary uranium deposits, Um Ara area, south Eastern Desert, Egypt. J. Afr. Earth Sci. 32, 317–323.

El-Dokouny, H.A., Watanabe, Y., Mahmoud, A.S., Dawoud, M., 2023. Geochemistry and petrogenesis of late Neoproterozoic Nuweibi and Atawi rare metals bearing granites, central Eastern Desert, Egypt. J. Afr. Earth Sci. 206, 105023.

El-Dosouky, A.M., El-Qassas, R.A.Y., Pour, A.B., Mohamed, H., Sekandari, M., 2021. Integration of ASTER satellite imagery and 3D inversion of aeromagnetic data for deep mineral exploration. Adv. Space Res. 68, 3641–3662.

El-Dosouky, A.M., Eleraki, M., Mansour, A., Saada, S.A., Zamzam, S., 2024. Geological controls of mineralization occurrences in the Egyptian Eastern Desert using advanced integration of remote sensing and magnetic data. Sci. Rep. 14, 16700.

El-Dosouky, A.M., Pham, L.T., Abdelrahman, K., Fnais, M.S., Gomez-Ortiz, D., 2022. Mapping structural features of the Wadi Umm Dulfah area using aeromagnetic data. J. King Saud Univ. 34, 101803.

El-Dosouky, A.M., Sehsah, H., Elkhateeb, S.O., Pour, A.B., 2020. Integrating aeromagnetic data and Landsat-8 imagery for detection of post-accretionary shear zones controlling hydrothermal alterations: the Allaqi-Heiani Suture zone, South Eastern Desert, Egypt. Adv. Space Res. 65, 1008–1024.

El-Kammar, A.E., El-Afandy, A.H., Nasr, T., Coltorti, M., Casetta, F., 2021. Geochemical constraints and uranium potential of the younger granitic rocks in El Maghrbia area, Central Eastern Desert, Egypt. Acta Geochim. 40, 623–639.

El-Kammar, A.M., El-Hazik, N., Mahdi, M., Aly, N., 1997. Geochemistry of accessory minerals associated with radioactive mineralisation in the central Eastern Desert, Egypt. J. Afr. Earth Sci. 25, 237–252.

El-Leil, I.A.A., Tolba, A.S., Omar, S.A.M., El-Feky, M.G., Bakiet, M.H., Awad, H.A., 2015. Radioactive mineralization of el-missikat granite; one of the most important occurrence, Eastern Desert, Egypt. Int. J. Innov. Sci. Eng. Technol. 2, 83–100.

El-Qassas, R.A.Y., Abu-Donia, A.M., Omar, A.E.A., 2023. Delineation of hydrothermal alteration zones associated with mineral deposits, using remote sensing and airborne geophysics data. A case study: el-Bakriya area, Central Eastern Desert, Egypt. Acta Geod. Geophys. 58, 71–107.

El-Sherif, A.M., 2013. Mineralogical characterization of the alteration facies at gabal el-missikat area, central Eastern Desert, Egypt. Nucl. Sci. Sci. J. 2, 1–21.

El Mezayen, A.M., Heikal, M.A., Abu Zeid, I.K., Omar, S.A., El-Feky, M.G., Lasheen, E.S.R., 2017. Petrography, geochemistry and radioactivity of El-Gidami granitic rocks, central eastern desert, Egypt. Al-Azhar Bullet. Sci. Confer. 9, 25–40.

Elkhateeb, S.O., Abdellatif, M.A.G., 2018. Delineation potential gold mineralization zones in a part of Central Eastern Desert, Egypt using Airborne Magnetic and Radiometric data. NRIAG J. Astron. Geophys. 7, 361–376.

Elsaid, M., Aboelkhair, H., Dardier, A., Hermas, E., Minoru, U., 2014. Processing of multispectral ASTER data for mapping alteration minerals zones: as an aid for uranium exploration in Elmissikat-Eleridiya granites, Central Eastern Desert, Egypt. Open Geol. J. 8.

Frutuoso, R., Lima, A., Teodoro, A.C., 2021. Application of remote sensing data in gold exploration: targeting hydrothermal alteration using Landsat 8 imagery in northern Portugal. Arabian J. Geosci. 14, 1–18.

Ge, W., Cheng, Q., Jing, L., Armenakis, C., Ding, H., 2018a. Lithological discrimination using ASTER and Sentinel-2A in the Shibanjing ophiolite complex of Beishan orogenic in Inner Mongolia, China. Adv. Space Res. 62, 1702–1716.

Ge, W., Cheng, Q., Tang, Y., Jing, L., Gao, C., 2018b. Lithological classification using Sentinel-2A data in the Shibanjing ophiolite complex in Inner Mongolia, China. Remote Sens. 10, 638.

Ghoneim, M.M., Abdel Gawad, A.E., El-Dokouny, H.A., Dawoud, M., Panova, E.G., El-Lithy, M.A., Mahmoud, A.S., 2024. Petrogenesis and geodynamic evolution of A-type granite bearing rare metals mineralization in Egypt: insights from geochemistry and mineral chemistry. Minerals 14, 583.

Ghoneim, S.M., Ali, H.F., Abdelrahman, K., Fnais, M.S., Lala, A.M.S., 2024. Integrating remote sensing and geophysical data for mapping potential gold mineralization localities at Abu Marawat area, central Eastern Desert, Egypt. Sci. Rep. 14, 18273.

Ghoneim, S.M., Yehia, M.A., Salem, S.M., Ali, H.F., 2022. Integrating remote sensing data, GIS analysis and field studies for mapping alteration zones at Wadi Saqia area, central Eastern Desert, Egypt. Egypt. J. Remote Sens. Sp. Sci. 25, 323–336.

Hassaan, M.M., Omar, S.A., Khalil, A.E., Shahin, T.M., El-Naggar, I.M., Sayyed, M.I., Hanfi, M.Y., 2022. Prognostic exploration of UF-Au-Mo-W younger granites for geochemical pathfinders, genetic affiliations, and tectonic setting in el-erediya-el-missikat province, Eastern Desert, Egypt. Minerals 12, 518.

Hassan, S.M., Ramadan, T.M., 2015. Mapping of the late Neoproterozoic Basement rocks and detection of the gold-bearing alteration zones at Abu Marawat-Semna area, Eastern Desert, Egypt using remote sensing data. Arabian J. Geosci. 8, 4641–4656.

Hassan, S.M., Youssef, M.A.S., Gabr, S.S., Sadek, M.F., 2022. Radioactive mineralization detection using remote sensing and airborne gamma-ray spectrometry at Wadi Al-Miyah area, Central Eastern Desert, Egypt. Egypt. J. Remote Sens. Sp. Sci. 25, 37–53.
Holden, E.-J., Dentith, M., Kovesi, P., 2008. Towards the automated analysis of regional aeromagnetic data to identify regions prospective for gold deposits. Comput. Geosci. 34, 1505–1513.
Hu, B., Xu, Y., Wan, B., Wu, X., Yi, G., 2018. Hydrothermally altered mineral mapping using synthetic application of Sentinel-2A MSI, ASTER and Hyperion data in the Duolong area, Tibetan Plateau, China. Ore Geol. Rev. 101, 384–397.
Hussein, H.A., Hassan, M.A., El-Tahir, M.A., Abou-Deif, A., 1986. Uranium-bearing siliceous veins in younger granites. Eastern Desert, Egypt. No. IAEA-TECDOC–361.
Hussein, H.A.M., Sayyah, T.A., 1992. Uranium Potential of the Younger Granites of Egypt.
Hyvärinen, A., Oja, E., 2000. Independent component analysis: algorithms and applications. Neural Netw. 13, 411–430.
Johnson, P.R., Andresen, A., Collins, A.S., Fowler, A.R., Fritz, H., Ghebreab, W., Kusky, T., Stern, R.J., 2011. Late Cryogenian–Ediacaran history of the Arabian–Nubian Shield: a review of depositional, plutonic, structural, and tectonic events in the closing stages of the northern East African Orogen. J. Afr. Earth Sci. 61, 167–232.
Johnson, P.R., Woldehaimanot, B., 2003. Development of the arabian-nubian Shield: perspectives on accretion and deformation in the northern East African orogen and the assembly of Gondwana. Geol. Soc. London, Spec. Publ. 206, 289–325.
Kassas, E., Bakhit, F.S., 1989. Geology of Wadi atalla-el Missikat area. Eastern Desert, Egypt.
Lee, T.-W., Girolami, M., Bell, A.J., Sejnowski, T.J., 2000. A unifying information-theoretic framework for independent component analysis. Comput. Math. Appl. 39, 1–21.
Loizzo, R., Daraio, M., Guarini, R., Longo, F., Lorusso, R., Dini, L., Lopinto, E., 2019. Prisma mission status and perspective. In: IGARSS 2019-2019 IEEE International Geoscience and Remote Sensing Symposium, pp. 4503–4506.
Mahmoud, A.S., Dyakonov, V.V., Kotelnikov, A.E., Dawoud, M., El-Dokouny, H.A., 2021. Vertical zoning and geochemical anomaly fields of the hamama gold deposit in the central part of Egypt's Eastern Desert. Geol. Ore Depos. 63, 156–171.
Mamouch, Y., Attou, A., Miftah, A., Ouchchen, M., Dadi, B., Achkouch, L., Et-tayea, Y., Allaoui, A., Boualoul, M., Randazzo, G., others, 2022. Mapping of hydrothermal alteration zones in the Kelâat M'Gouna region using airborne gamma-ray spectrometry and remote sensing data: mining implications (eastern anti-atlas, Morocco). Appl. Sci. 12, 957.
Meyer, C., 1967. Wall rock alteration. Geochemistry Hydrothermal Ore Depos.
Miller, H.G., Singh, V., 1994. Potential field tilt—a new concept for location of potential field sources. J. Appl. Geophys. 32 (2–3), 213–217.
Mishra, G., Govil, H., Guha, A., Kumar, H., Kumar, S., Mukherjee, S., 2022. Comparative evaluation of airborne AVIRIS-NG and spaceborne PRISMA hyperspectral data in identification and mapping of altered/weathered minerals in Jahazpur, Rajasthan. Adv. Space Res.
Nafigin, I.O., Ishmukhametova, V.T., Ustinov, S.A., Minaev, V.A., Petrov, V.A., 2022. Geological and mineralogical mapping based on statistical methods of remote sensing data processing of landsat-8: a case study in the Southeastern Transbaikalia, Russia. Sustainability 14, 9242.
Osman, A.M., Salman, A.B., El-Mansi, M.M., Abdel Ghani, I.M., Abdallah, S.M., 2005. Mineralogy and uranium distribution in some subsurface sections from El-Missikat and El-Erediya uranium occurrences, Eastern Desert, Egypt. Delta J. Sci. 29, 18–38.
Peyghambari, S., Zhang, Y., 2021. Hyperspectral remote sensing in lithological mapping, mineral exploration, and environmental geology: an updated review. J. Appl. Remote Sens. 15, 31501.
Pour, A.B., Hashim, M., 2015a. Structural mapping using PALSAR data in the central gold belt, Peninsular Malaysia. Ore Geol. Rev. 64, 13–22.
Pour, A.B., Hashim, M., 2015b. Integrating PALSAR and ASTER data for mineral deposits exploration in tropical environments: a case study from Central Belt, Peninsular Malaysia. Int. J. Image Data Fusion 6, 170–188.
Pour, A.B., Hashim, M., 2012. The application of ASTER remote sensing data to porphyry copper and epithermal gold deposits. Ore Geol. Rev. 44, 1–9.
Pour, A.B., Park, Y., Park, T.-Y.S., Hong, J.K., Hashim, M., Woo, J., Ayoobi, I., 2019. Evaluation of ICA and CEM algorithms with Landsat-8/ASTER data for geological mapping in inaccessible regions. Geocarto Int. 34, 785–816.
Pournamdari, M., Hashim, M., Pour, A.B., 2014a. Application of ASTER and Landsat TM data for geological mapping of esfandagheh ophiolite complex, Southern Iran. Resour. Geol. 64, 233–246.
Pournamdari, M., Hashim, M., Pour, A.B., 2014b. Spectral transformation of ASTER and Landsat TM bands for lithological mapping of Soghan ophiolite complex, south Iran. Adv. Space Res. 54, 694–709.
Ranjbar, H., 2011. Application of spectral analysis in mapping hydrothermal alteration of the Northwestern part of the kerman cenozoic magmatic arc, Iran. J. Sci. Islam. Repub. Iran 22, 221–238.
Raslan, M.F., 2021. Au-bearing Pyrite and Pt-Re-Rich Molybdenite in the Sulphide Mineralized Younger Granites in the Eastern Desert of Egypt.
Raslan, M.F., 2009. Occurrence of uraniferous iron grains at gabal gattar, el missikat and el erediya granites in Eastern Desert of Egypt. Resour. Geol. 59, 99–105.
Reid, A.B., Allsop, J.M., Granser, H., Millett, A.T., Somerton, I.W., 1990. Magnetic interpretation in three dimensions using Euler deconvolution. Geophysics 55 (1), 80–91. .
Ridley, J., 2013. Ore Deposit Geology. Cambridge University Press.
Sabins, F.F., 1999. Remote sensing for mineral exploration. Ore Geol. Rev. 14, 157–183.
Saleh, A., Gabr, S.S., 2024. Application of magnetic data and satellite spectral imaging in identifying gold mineralization zones and its associated subsurface structures at Fawakheir-Attala area, Central Eastern Desert, Egypt. Environ. Earth Sci. 83, 500.
Salem, S.M., 2013. Detecting of new alteration zones for gold exploration at the Barramiya District, Central Eastern Desert of Egypt using ASTER data and geological field verification. Arab. J. Geosci. AJGS-D-12-00632 4, 161–176.
Shahin, H.A.A., Emad, B.M., Masoud, M.S., 2021. Uranium and rare metal mineralization in the el sela and qash amir granitic intrusions, south Eastern Desert, Egypt. J. Asian Earth Sci. X 6, 100066.
Shalaby, M.H., Bishta, A.Z., Roz, M.E., El Zalaky, M.A., 2010. Integration of geologic and remote sensing studies for the discovery of uranium mineralization in some granite plutons, Eastern Desert, Egypt. J. King Abdulaziz Univ. - Earth Sci. 21, 125.
Shebl, A., Abdellatif, M., Elkhateeb, S.O., Csámer, Á., 2021. Multisource data analysis for gold potentiality mapping of Atalla area and its environs, Central Eastern Desert, Egypt. Minerals 11, 641.
Shebl, A., Abriha, D., Dawoud, M., Ali, M.A.H., Csámer, Á., 2024. PRISMA vs. Landsat 9 in lithological mapping- a K-fold Cross-Validation implementation with Random Forest. Egypt. J. Remote Sens. Sp. Sci. 27, 577–596.
Shebl, A., Abriha, D., Fahil, A.S., El-Dokouny, H.A., Elrasheed, A.A., Csámer, Á., 2023. PRISMA hyperspectral data for lithological mapping in the Egyptian Eastern Desert: evaluating the support vector machine, random forest, and XG boost machine learning algorithms. Ore Geol. Rev., 105652.
Stern, R.J., 2002. Crustal evolution in the East African Orogen: a neodymium isotopic perspective. J. Afr. Earth Sci. 34, 109–117.
Tharwat, A., 2021. Independent component analysis: an introduction. Appl. Comput. Inform. 17, 222–249.
Yousef, M.H.M., 2019. Delineation of radiometric anomalies and conductive zones using gamma-ray spectrometric and electromagnetic methods, east Gabal El-Urf area, Northern Eastern Desert, Egypt. Appl. Radiat. Isot. 153, 108822.